



HAL
open science

A post-New Horizons Global climate model of Pluto including the N₂, CH₄ and CO cycles

F. Forget, T. Bertrand, M. Vangvichith, J. Leconte, E. Millour, E. Lellouch

► **To cite this version:**

F. Forget, T. Bertrand, M. Vangvichith, J. Leconte, E. Millour, et al.. A post-New Horizons Global climate model of Pluto including the N₂, CH₄ and CO cycles. *Icarus*, 2016, 287, pp.54-71. 10.1016/j.icarus.2016.11.038 . hal-01427123

HAL Id: hal-01427123

<https://hal.sorbonne-universite.fr/hal-01427123>

Submitted on 5 Jan 2017

HAL is a multi-disciplinary open access archive for the deposit and dissemination of scientific research documents, whether they are published or not. The documents may come from teaching and research institutions in France or abroad, or from public or private research centers.

L'archive ouverte pluridisciplinaire **HAL**, est destinée au dépôt et à la diffusion de documents scientifiques de niveau recherche, publiés ou non, émanant des établissements d'enseignement et de recherche français ou étrangers, des laboratoires publics ou privés.

A post-New Horizons Global climate model of Pluto including the N₂, CH₄ and CO cycles

F. Forget^{a,*}, T. Bertrand^a, M. Vangichith^a, J. Leconte^{a,**}, E. Millour^a, E. Lellouch^b

^a *Laboratoire de Météorologie Dynamique (LMD/IPSL), CNRS, Sorbonne Universités, UPMC Univ Paris 06, Paris, France*

^b *Laboratoire d'Etudes Spatiales et d'Instrumentation en Astrophysique (LESIA), Observatoire de Paris, CNRS, UPMC, Université Paris Diderot, F-92195 Meudon, France*

Abstract

We have built a new 3D Global Climate Model (GCM) to simulate Pluto as observed by New Horizons in 2015. All key processes are parametrized on the basis of theoretical equations, including atmospheric dynamics and transport, turbulence, radiative transfer, molecular conduction, as well as phases changes for N₂, CH₄ and CO. Pluto's climate and ice cycles are found to be very sensitive to model parameters and initial states. Nevertheless, a reference simulation is designed by running a fast, reduced version of the GCM with simplified atmospheric transport for 40,000 Earth years to initialize the surface ice distribution and sub-surface temperatures, from which a 28-Earth-year full GCM simulation is performed. Assuming a topographic depression in a Sputnik-planum (SP)-like crater on the anti-Charon hemisphere, a realistic Pluto is obtained, with most N₂ and CO ices accumulated in the crater, methane frost covering both hemispheres except for the equatorial regions, and a surface pressure near 1.1 Pa in 2015 with an increase between 1988 and 2015, as reported from stellar occultations. Temperature profiles are in qualitative agreement with the observations. In particular, a cold atmospheric layer is obtained in the lowest kilometers above Sputnik Planum, as observed by New Horizons's REX experiment. It is shown to result from the combined effect of the topographic depression and N₂ daytime sublimation. In the reference simulation with surface N₂ ice exclusively present in Sputnik Planum, the global circulation is only forced by radiative heating gradients and remains relatively weak. Surface winds are locally induced by topography slopes and by N₂ condensation and sublimation around Sputnik Planum. However, the circulation can be more intense depending on the exact distribution of surface N₂ frost. This is illustrated in an alternative simulation with N₂ condensing in the South Polar regions and N₂ frost covering latitudes between 35°N and 48°N. A global condensation flow is then created, inducing strong surface winds everywhere, a prograde jet in the southern high latitudes, and an equatorial superrotation likely forced by barotropic instabilities in the southern jet. Using realistic parameters, the GCM predict atmospheric concentrations of CO and CH₄ in good agreement with the observations. N₂ and CO do not condense in the atmosphere, but CH₄ ice clouds can form during daytime at low altitude near the regions covered by N₂ ice (assuming that nucleation is efficient enough). This global climate model can be used to study many aspects of the Pluto environment. For instance, organic hazes are included in the GCM and analysed in a companion paper (Bertrand and Forget, *Icarus*, this issue).

1. Introduction

Only six terrestrial bodies in our solar system (Venus, Earth, Mars, Titan, Triton, Pluto) possess an atmosphere thick enough to be governed by the same equations of meteorology as on Earth, or able to support clouds or hazes. Among them, Pluto presents a unique case, with an atmosphere significantly warmer than the underlying surface,

*Corresponding author. E-mail: forget@lmd.jussieu.fr

**now at Laboratoire d'Astrophysique de Bordeaux, Univ. Bordeaux, F-33270 Floirac, France

5 long radiative timescales, and a circulation dominated by condensation/sublimation process of the main atmospheric
6 component. Studying this exotic case can provide new insight into the physics of terrestrial atmosphere.

7 The observations made by the New Horizons spacecraft have revealed the nature of the surface of Pluto and have
8 provided unprecedented constraints on the state of the atmosphere in 2015 (Stern et al., 2015; Gladstone et al., 2016;
9 Grundy et al., 2016; Moore et al., 2016). Within that context, it is now interesting to test our ability to create a 3D
10 numerical simulator of the Pluto climate system, analogous to the climate models already used on the Earth as well as
11 on Mars, Venus and Titan. Conversely, the output of such a Global Climate Model is useful to interpret the available
12 atmospheric measurements, and can even shed light on some geological observations.

13 *1.1. Pluto's ices and atmosphere observations*

14 The presence of a significant atmosphere on Pluto was demonstrated in 1988 by observing a stellar occultation
15 by Pluto (Hubbard et al., 1988; Elliot et al., 1989). This atmosphere was predicted to be mainly composed of molec-
16 ular nitrogen in vapour-pressure equilibrium with N₂ ice deposits observed on the surface. In 2015, New Horizons
17 determined a pressure of about 10 μ bar, i.e. 1 Pa (Hinson et al., 2015b; Gladstone et al., 2016). However, a series
18 of stellar occultations conducted since 1988 have shown that the pressure at a specific reference level (e.g. 1275 km
19 from Pluto's center) has increased by a factor of three during that period (Elliot et al., 2003a,b; Olkin et al., 2015),
20 suggesting a similar rise of the surface pressure.

21 Prior to the New Horizons flyby, spectroscopic observations had demonstrated that, in addition to N₂ ice, Pluto's
22 surface is covered by patches of CH₄ and CO ices (Owen et al., 1993; Douté et al., 1999; Grundy et al., 2013).
23 New Horizons was able to map these ices and revealed that the main reservoir was a thick ice cap informally named
24 Sputnik Planum, with thinner N₂ frost covering the mid-northern latitudes and CH₄ frost possibly everywhere except
25 in the equatorial dark regions (Grundy et al., 2016).

26 Accordingly, CH₄ and CO gas were observed from Earth to be present in present-day Pluto's atmosphere (Young
27 et al., 1997; Lellouch et al., 2009, 2011a, 2015, 2016), with, during the 2008-2012 period, volume mixing ratios near
28 0.05% for CO and 0.5% for CH₄. (Lellouch et al., 2011a, 2015). CH₄ has also been observed by New Horizons Alice
29 spectrograph. in 2015 and estimated to range between 0.6 and 0.84 % in the lower atmosphere (Gladstone et al.,
30 2016). Using the hydrostatic equation, atmospheric temperature profiles have been derived from vertical density
31 profiles retrieved from Earth-based stellar occultations (Elliot et al., 1989, 2003b, 2007; Person et al., 2008; Young
32 et al., 2008; Dias-Oliveira et al., 2015; Sicardy et al., 2016), and from radio and solar occultations performed by
33 New Horizons (Hinson et al., 2015b; Gladstone et al., 2016). The latest stellar occultations and New Horizon's
34 data consistently show that the temperature profile is characterized by a steep temperature gradient in the lower
35 atmosphere, with temperature increasing from surface values (38 to 55 K) at 0 km to about 110 K at 20 km. This

36 has been interpreted as resulting from the absorption of near-infrared solar radiation by gaseous methane (Yelle and
37 Lunine, 1989; Strobel et al., 1996). Above 30 km, the temperature appears to decrease with altitude to reach about
38 70-80 K around 200 km (Dias-Oliveira et al., 2015; Gurwell et al., 2015; Gladstone et al., 2016). Such a structure
39 requires infrared-cooling species acting only at a specific altitude range. C_2H_2 and HCN – respectively detected by
40 New Horizons (Gladstone et al., 2016) and from the ground (Lellouch et al., 2016) – have been proposed, but the
41 details of exactly how Pluto's upper atmosphere is being cooled remains poorly understood (Gladstone et al., 2016).
42 Finally, stellar occultation observations suggest that the temperature profiles are affected by oscillation that can be
43 related to gravity waves or thermal tides (Elliot et al., 2003b; Person et al., 2008; Toigo et al., 2010).

44 *1.2. 3D Modelling of the Pluto surface-atmosphere system*

45 To improve our understanding of the complex Pluto surface-atmosphere system, we have built a new Global
46 Climate Model (GCM) including a full simulation of the nitrogen, methane, and carbon monoxide cycles. This GCM
47 computes the temporal evolution of the variables which control the meteorology and the climate of the planet in
48 different points of a 3D grid covering the entire atmosphere. On the Earth, GCMs have been applied to weather
49 forecasting and climate change projections. Because these models are almost entirely built on physical equations
50 (rather than empirical parameters), several teams around the world have been able to successfully adapt them to the
51 other terrestrial planets or satellites that have a solid surface and a thick enough atmosphere. The Pluto GCM presented
52 in this paper is derived from the LMD Global Climate Model of planet Mars (Forget et al. 1999) which has been used
53 for numerous applications including simulating CO_2 ice caps analogous to Pluto's N_2 ice caps (Forget et al. 1998),
54 the thermosphere (Gonzalez-Galindo et al., 2009), photochemistry (Lefevre et al. 2008) or paleoclimatology (e.g.
55 Forget et al. 2006). The LMD GCM has been adapted to Venus (Lebonnois et al., 2010) and Titan (Hourdin et al.
56 1995, Lebonnois et al. 2012). All these GCMs have been able to predict or accurately reproduce the observed thermal
57 structure and circulation, giving us some confidence in its ability to predict the characteristics of the Pluto atmosphere
58 in spite of the scarcity of observations.

59 For Pluto, after the simplified General Circulation Model (without phase changes) presented by Zalucha and
60 Michaels (2013) for Pluto and Triton, a realistic model was developed by Toigo et al. (2015) a few months before
61 the New Horizons encounter. This model includes a “robust treatment of nitrogen volatile transport”, and initializes
62 the full GCM using a two dimensional surface volatile exchange model and a one-dimensional radiative-convective-
63 convective model. In this paper we present a new model with a different origin and which benefits from the New
64 Horizons observations. We include an improved N_2 condensation-sublimation scheme, the full CO and CH_4 cycles,
65 and explore the effect of topography. Nevertheless, we use an analogous strategy for the initialization.

66 In Sections 2, we provide a detailed description of the different components of our Pluto Global Climate Model,
67 and in Section 3 we discuss how the different model parameters were chosen and how the 3D GCM is initialized for
68 our two baseline simulations. The model results for temperature and winds and for the CH₄ and CO cycles are then
69 presented in Sections 4 and 5, before the conclusion.

70 2. Model description

71 2.1. Generalities

72 As mentioned above, our Pluto Global Climate Model is derived from the LMD Mars GCM (Forget et al., 1999) ,
73 with several new parameterizations. Its core is a hydrodynamical code dedicated to the temporal and spatial integration
74 of the equations of hydrodynamics, used to compute the large scale atmospheric motions and the transport. The
75 equations are solved using a finite difference scheme on an “Arakawa C” grid (Arakawa and Lamb, 1977). Such a
76 scheme is equally valid for the Earth, Mars or Pluto. Therefore the hydrodynamical core has not been modified for
77 Pluto. While the estimated surface pressure on Pluto (10 μ bar or 1 Pa) is much lower than on the Earth or even on
78 Mars, the atmosphere is thick enough to be modeled with the primitive equations of meteorology used in the model.
79 In fact, it is generally found that GCMs dynamical cores are valid almost up to the exobase. For instance, on Mars our
80 dynamical core has been used successfully up to the thermosphere at pressures lower than 10⁻⁷ Pa (González-Galindo
81 et al., 2009).

82 In this paper, we present simulations with a horizontal grid of 32×24 points to cover the planet, that is a grid-point
83 spacing of 7.5° latitude by 11.25° longitude. The corresponding spatial resolution is of about 150 km, which is equal
84 or better to the typical resolution used in planetary GCMs, and which is sufficient to resolve possible planetary waves.
85 We also performed simulations with a doubled resolution (64×48) and even an experimental run with a 360×180 grid,
86 and did not find any fundamental differences in the results that could change the conclusions of this paper. Their
87 analysis is out of the scope of this paper and will be presented in a future article, in which we will take into account
88 a more realistic topography. In the vertical, the model uses the terrain-following “sigma” coordinate system in finite
89 difference form (i.e. each layer is defined by a constant value of the ratio pressure divided by surface pressure). 25
90 levels are typically used. In the baseline model, most of the levels are located in the first 15 km to obtain a good
91 resolution close to the surface, in the boundary layer. The altitude of the first mid-layers are 7 m, 15 m, 25 m, 40 m,
92 80 m etc.. Above 10 km, the resolution is about one scale height, with the upper pressure level equal to 0.007 times
93 surface pressure, i.e. up to 250 km. (Note that in a companion paper dedicated to the study of atmospheric hazes
94 Bertrand and Forget (2016), the top of the model is extended to about 600 km to include the altitudes of methane
95 photolysis).

96 2.2. Radiative transfer

97 The incident insolation upon each modeled atmospheric column is calculated at each timestep, taking into account
98 the variation of the Pluto-Sun distance throughout its orbit, the seasonal inclination and the diurnal cycle.

99 While N_2 is the major constituent of the atmosphere of Pluto, its radiative effects are neglected in the lower
100 atmosphere since N_2 is transparent at solar and infrared wavelengths. Nevertheless we account for (1) the radiative
101 heating and cooling by CH_4 , which can vary in space and time depending of the results of the methane cycle model
102 (see section 2.8) (2) cooling by the thermal infrared rotational lines of CO, which volume mixing ratio is prescribed
103 at 0.05 % everywhere (Lellouch et al., 2011a, 2016) and 3) the effect of other infrared emitting species in altitude.

104 2.2.1. Radiative transfer through CH_4 and CO

105 For CH_4 and CO, we use a correlated k -distribution radiative transfer model, with 17 spectral bands in the thermal
106 infrared and 23 for solar wavelengths. The bands are designed to well represent the 1.6, 2.3 and 3.3 μm CH_4 vibra-
107 tional bands in the near infrared as well as the 7.6 μm CH_4 emission band in the thermal infrared. To calculate the
108 k absorption coefficients in each bands, high resolution line-by-line spectra combining CO and CH_4 were computed
109 from the HITRAN 2012 database using the open-source “kspectrum” tool. Spectra and k coefficients were calculated
110 to fill a look up table matrix (from which the k coefficients are interpolated by the GCM in each spectral band) compris-
111 ing 8 temperatures \times 7 log-pressure \times 7 CH_4 volume mixing ratio grid, with $T = \{30, 40, 50, 70, 90, 110, 150, 200\}$ K,
112 $p = \{10^{-4}, 10^{-3}, 10^{-2}, 10^{-1}, 1, 10, 100\}$ Pa, and $[CH_4] = \{10^{-4}, 10^{-3}, 5 \times 10^{-3}, 10^{-2}, 5 \times 10^{-2}, 10^{-1}, 5 \times 10^{-1}\}$ kg/kg. We
113 found that no less than 33 points were needed for the g -space integration to get accurate results throughout the matrix
114 space (g is the cumulated distribution function of the absorption data for each band).

115 2.2.2. Non Local Thermal Equilibrium processes

116 In the low-pressure, low temperature Pluto environment, a major difficulty (and therefore uncertainty) in the
117 radiative transfer calculations results from the fact that the methane lines can be far from Local Thermal Equilibrium
118 (LTE). It is not the case of CO rotational lines which are assumed to remain in LTE for the pressure levels that we
119 model in this paper.

120 To account for non-LTE effects for the 7.6 μm CH_4 band, we modify the LTE cooling rates obtained with the
121 correlated k -distribution radiative transfer model as in Strobel et al. (1996). However, the total CH_4 cooling rates we
122 obtain are found to be much lower than shown in Strobel et al. (1996), and significantly smaller than the CO cooling
123 rates. This is also found in recent models from the same authors (D. Strobel, personal communication) The difference
124 is thought to result from the updated spectroscopic database (HITRAN 2012 vs HITRAN 1986) and the fact that the

125 temperatures used in Strobel et al. (1996) are larger than here. The uncertainties on the NLTE calculations for the
 126 $7.6 \mu\text{m}$ CH_4 band have thus a limited effect on our results.

127 For the near-infrared solar bands, we first reproduced the calculations from Strobel et al. (1996) updated by Za-
 128 lucha et al. (2011) for each of the 2.3 and $3.3 \mu\text{m}$ bands. We had no information on the $1.6 \mu\text{m}$ band. Within that
 129 context, and given the overall uncertainty in the NLTE calculations (Boursier et al., 2003), we authorized some empir-
 130 ical modifications of the theoretical NLTE variations with atmospheric density (while keeping the theoretical shape)
 131 to adjust the heating rates in order to get temperatures closer to the thermal structure observed by New Horizons.
 132 Therefore, the ability of our GCM to roughly reproduce the observed mean thermal structure should not be regarded
 133 as a success of our radiative transfer model. In practice, we multiply the total CH_4 heating rate provided by the LTE
 134 radiative transfer code by a vertically varying non-LTE efficiency coefficient ϵ_{NLTE} .

$$\epsilon_{\text{NLTE}} = 0.1 + \frac{0.9}{1 + \rho_{.55}/\rho}, \quad (1)$$

135 with ρ the atmospheric density (kg m^{-3}), and $\rho_{.55}$ the reference density for which $\epsilon_{\text{NLTE}} = 0.55$. After tuning, we set
 136 $\rho_{.55} = 2 \times 10^{-6} \text{ kg m}^{-3}$.

137 2.2.3. Additional radiative coolers

138 As mentioned in the introduction, the presence of radiatively cooling species at a specific altitude has been sug-
 139 gested to explain the decrease of temperature above 30 km (Dias-Oliveira et al., 2015; Gladstone et al., 2016). Using
 140 the cooling-to-space approximation, we phenomenologically represent this effect with the following cooling rate for
 141 pressures below 0.12 Pa :

$$\frac{\partial T}{\partial t} = -5 \times 10^{-11} B(\lambda_0, T) \quad (2)$$

142 with T the atmospheric temperature (K) and $B(\lambda_0, T)$ the Planck function (in $\text{W m}^{-2} \mu\text{m}^{-1} \text{sr}^{-1}$) at wavelength λ_0 .
 143 We use $\lambda_0 = 14 \mu\text{m}$ since the main emission bands of the most likely cooling species C_2H_2 and HCN (Gladstone et al.,
 144 2016) are respectively centered at 13.7 and $14.05 \mu\text{m}$ (we here neglect the rotational bands of HCN at submillimeter
 145 wavelengths). The value -5×10^{-11} was chosen to simulate a moderate cooling yielding temperatures below 90 K in
 146 our reference simulation.

147 2.3. Atmospheric molecular thermal conduction and viscosity

148 We account for the effect of molecular conduction on temperature and molecular viscosity on winds. Both pro-
 149 cesses are governed by similar equations. Assuming the plane-parallel approximation, for thermal conduction we

150 get:

$$\frac{\partial T}{\partial t} = \frac{1}{\rho c_p} \frac{\partial}{\partial z} \left(k \frac{\partial T}{\partial z} \right) \quad (3)$$

151 where T is the temperature (K), ρ the density (kg m^{-3}) and k the thermal conduction coefficient ($\text{J m}^{-1} \text{s}^{-1} \text{K}^{-1}$),
 152 expressed as $k = k_0 T^s$, with $k_0 = 5.63 \times 10^{-5} \text{ J m}^{-1} \text{s}^{-1} \text{K}^{-(1+s)}$ and $s = 1.12$ (Hubbard et al., 1990).

153 For molecular viscosity:

$$\frac{\partial S}{\partial t} = \frac{1}{\rho} \frac{\partial}{\partial z} \left(\mu \frac{\partial S}{\partial z} \right) \quad (4)$$

154 where S stands for the components of the horizontal wind (m s^{-1}) and μ is the coefficient of molecular viscosity
 155 ($\text{kg m}^{-1} \text{s}^{-1}$), that is related to the thermal conduction coefficient by $k = \frac{1}{4}[9c_p - 5(c_p - R)]\mu$. Given its similarity, both
 156 equations are discretized and solved using the same implicit numerical schemes.

157 2.4. Surface temperatures and thermal conduction in the subsurface

158 Surface temperature evolution T_s is governed by the balance between solar insolation, thermal emission in the
 159 infrared, latent heat exchanges (see section 2.6), sensible heat flux from the atmosphere (usually negligible on Pluto,
 160 but taken into account in the model) and thermal conduction in the soil. On a weakly irradiated body like Pluto, the
 161 radiative fluxes are small compared to the internal heat stored in the ground. In particular, the subsurface heat stored
 162 during one season can play a major role in the control of the surface temperature at the opposite season.

163 The heat flux from and to the subsurface is computed using a classical model of the evolution of the subsurface
 164 temperatures T as a function of time t and depth z . It satisfies the following equation:

$$C \frac{\partial T}{\partial t} = \frac{\partial}{\partial z} \left[\lambda \frac{\partial T}{\partial z} \right] \quad (5)$$

165 where λ is the heat conductivity of the ground, ($\text{J s}^{-1} \text{m}^{-1} \text{K}^{-1}$) and C the ground volumetric specific heat (J m^{-3}
 166 K^{-1}). This equation is solved using a finite differences approach and an implicit Euler scheme. The key parameter
 167 which controls the influence of the subsurface heat storage and conduction on the surface temperature is the thermal
 168 Inertia $I = \sqrt{\lambda C}$. In practice, we thus use I as the key model parameter, assuming a constant value for $C=10^6 \text{ J m}^{-3}$
 169 K^{-1} and making λ vary accordingly.

170 On Pluto the discretization requires a special attention compared to the Earth or Mars because one need to simul-
 171 taneously capture 1) the short period diurnal thermal waves in the near-surface, low thermal inertia terrain and 2) the
 172 much longer seasonal thermal waves which can penetrate deep in the high thermal inertia substrate. In this paper,

173 we assumed a relatively low diurnal thermal inertia $I_{\text{day}} = 50 \text{ J s}^{-1/2} \text{ m}^{-2} \text{ K}^{-1}$, slightly higher than the 20 to 30 SI
 174 range reported by Lellouch et al. (2011b) from their Spitzer data analysis. For the seasonal thermal inertia, we set
 175 $I_{\text{year}} = 800 \text{ J s}^{-1/2} \text{ m}^{-2} \text{ K}^{-1}$, which corresponds to a low porosity ice/rock-like substrate.

176 The skin depth of a thermal wave of period P (s) is:

$$\delta_P = \frac{I}{C} \sqrt{\frac{P}{\pi}} \quad (6)$$

177 The modeled diurnal and annual skin depths are thus 0.02 m and 40 m respectively. To represent this accurately,
 178 the subsurface is divided into $N = 22$ discrete layers, with a geometrically stretched distribution of layers with higher
 179 resolution near the surface and a coarser grid at depth:

$$z_k = z_1 2^{k-1} \quad (7)$$

180 where $z_1 = 1.414 \times 10^{-4} \text{ m}$ is the depth of the first layer. The deepest layer depth is thus near 300 m.

181 2.5. *Mixing in the boundary layer*

182 Turbulent mixing and convection are parameterized as in Forget et al. (1999). In practice, the boundary layer
 183 dynamics is accounted for by a Mellor and Yamada (1982) unstationary 2.5-level closure scheme, used to compute
 184 turbulent mixing coefficients induced by wind shears depending on the temperature profile stability and the evolution
 185 of turbulent kinetic energy. It is completed by a ‘‘convective adjustment’’ scheme which rapidly mixes the atmosphere
 186 in the case of unstable temperature profiles (rare on Pluto).

187 Turbulence and convection mix energy (potential temperature), momentum (wind), and tracers (gases and aerosols).
 188 In the surface layer, the turbulent surface flux is given by

$$F = \rho C_d U_1 (q_1 - q_0), \quad (8)$$

189 where q_1 and q_0 are the variable values in the first atmospheric layer and at the surface ($q_0 = 0$ for winds), U_1 is the
 190 horizontal wind velocity in the first layer, and C_d is the drag coefficient. Because of the small depth of the first layer
 191 z_1 , we assume that the wind profile in the first meters above the surface is logarithmic and not influenced by stability,
 192 and simply use

$$C_d = \left(\frac{\kappa}{\ln \frac{z_1}{z_0}} \right)^2 \quad (9)$$

193 where κ is the von Karman constant ($\kappa = 0.4$) and z_0 is the roughness coefficient, set to $z_0 = 0.01 \text{ m}$ everywhere like

194 in the Mars GCM (Forget et al., 1999).

195 Turbulent mixing is negligible outside the boundary layer (which is often shallow on Pluto because of the positive
196 lapse rate above the surface). In our GCM there is no other vertical “eddy diffusion” process. In particular, species
197 are only transported upwards by the large scale circulation.

198 2.6. N_2 Condensation and Sublimation

199 The condensation and sublimation of nitrogen ice must be carefully computed in the Pluto environment. The
200 amount of energy and the relative mass of the atmosphere involved in phases changes at each timestep can be very
201 significant. Locally, it not only changes the surface temperature and pressure, but it also modifies the structure of
202 the boundary layer by “pumping” the air when condensation occurs on the surface, and by releasing large amount of
203 cold, pure nitrogen (with no horizontal velocity) when N_2 sublimates. Our scheme is adapted from Forget et al. (1998).
204 However, we found it necessary to make several changes in the equations to better represent the intense condensation
205 and sublimation at the surface of Pluto.

206 The variation of the condensation temperature T_c with nitrogen partial pressure P_{N_2} is derived from the thermody-
207 namic relations computed by Fray and Schmitt (2009), taking into account the transition from the α to the β crystalline
208 form near 35.61 K (corresponding to $P_{N_2} = 0.53$ Pa):

$$\text{if } P_{N_2} < 0.53 \text{ Pa : } T_c = \left[\frac{1}{35.600} - \frac{296.925}{1.09L_{N_2}} \ln \left(\frac{P_{N_2}}{0.508059} \right) \right]^{-1} \quad (10)$$

$$\text{if } P_{N_2} > 0.53 \text{ Pa : } T_c = \left[\frac{1}{63.147} - \frac{296.925}{0.98L_{N_2}} \ln \left(\frac{P_{N_2}}{12557.} \right) \right]^{-1} \quad (11)$$

209 with $L_{N_2} = 2.5 \cdot 10^5 \text{ J kg}^{-1}$ the latent heat of condensation for nitrogen.

210 2.6.1. Surface Condensation and sublimation

211 The condensation and sublimation of nitrogen on the ground is primarily controlled by energy and mass conser-
212 vation. At a given timestep, if the surface temperature predicted by radiative and conductive balance T_0^* falls below
213 the condensation temperature at surface pressure T_{c0} , an amount δm_0 (kg m^{-2}) of N_2 condenses, releasing the latent
214 heat required to keep the solid-gas interface at the condensation temperature ($T_0 = T_{c0}$):

$$\delta m_0 = \frac{c_s}{(L_{N_2} + c_p(T_1 - T_{c0}))} (T_{c0} - T_0^*) \quad (12)$$

215 c_s is the surface heat capacity (in $\text{J m}^{-2} \text{K}^{-1}$), c_p the air specific heat at constant pressure (set to $1040 \text{ J kg}^{-1} \text{K}^{-1}$
 216 for N_2) and L_{N_2} the latent heat of N_2 ($2.5 \cdot 10^5 \text{ J kg}^{-1}$).

217 The term $c_p(T_1 - T_{c0})$ (J kg^{-1}) corresponds to the extra heat brought by the atmosphere (assumed to be at tem-
 218 perature T_1 in the first model layer) when cooled to the condensation temperature T_{c0} just above the surface. Because
 219 Pluto's lower atmosphere is a warm stratosphere lying just above a surface, we found that this term can be significant.
 220 With T_1 typically 10 K above T_{c0} when N_2 condenses in the topics, it reaches 4% of the latent heat. Conversely, when
 221 surface N_2 ice predicted temperature T_0^* is above the frost point T_{c0} , N_2 sublimates and δm_0 is negative:

$$\delta m_0 = \frac{c_s}{L_{\text{N}_2}}(T_{c0} - T_0^*) \quad (13)$$

222 We set $T_0 = T_{c0}$, unless all the local ground ice of mass m_0 (kg m^{-2}) completely sublimates. We then set $\delta m_0 = -m_0$
 223 and the new surface temperature is expressed as: $T_0 = T_0^* - L_{\text{N}_2} m_0 / c_s$. The formation or disappearance of nitrogen ice
 224 on the substrate is taken into account in the calculations of the surface albedo and emissivity.

225 2.6.2. Atmospheric Condensation and sublimation

226 In the atmosphere, things are, in theory, more complex. The condensation of a gas involves various microphysical
 227 processes: supersaturation, nucleation, crystal growth, sedimentation, etc... In our model, we have kept the detailed
 228 Mars GCM CO_2 ice scheme described in the appendix of Forget et al. (1998) and directly adapted it to N_2 ice. Su-
 229 persaturation is neglected and atmospheric condensation and sublimation are computed using energy conservation
 230 principles as above. We do not simulate the growth and transport of nitrogen ice particles. Instead, after condensing
 231 at a given model level, we assume that N_2 ice falls through the atmospheric layers located below it (where it can
 232 sublimate), possibly down to the ground within a model timestep.

233 Because the atmosphere is warmer than the surface most of the time, we have found that atmospheric condensation
 234 is a processes of little importance on Pluto as we model it with a 150 km resolution. In reality, ascending motions
 235 induced by local slopes or gravity waves could trigger condensation in N_2 ice covered regions. We will explore that
 236 in future versions of the model.

237 2.6.3. Computing mass, momentum and heat vertical fluxes induced by N_2 condensation and sublimation

238 The condensation and sublimation of nitrogen induce significant transport of air (mass, heat, momentum, tracers)
 239 through the model layers as well as to and from the surface. These processes must be taken into account on Pluto
 240 where an atmospheric layer of several tens of meters thick can undergo a phase change at each timestep. The numerical
 241 resolution of these processes in the “ σ ” vertical coordinates used in the GCM (see Section 2.1) is given in the appendix.

242 *2.7. Organic hazes*

243 New Horizons revealed the presence of extensive hazes thought to be primarily composed of organic particles
 244 indirectly produced by methane photolysis. Our GCM includes a model of the formation and transport of these
 245 particles. This model and its outputs are described and analyzed in a companion paper by Bertrand and Forget (2016),
 246 and not detailed here.

247 *2.8. Methane cycle and CH₄ ice clouds*

248 The 3D evolution of CH₄ on the surface and in gaseous and solid phase in the atmosphere is simulated taking
 249 into account 1) the condensation and sublimation at the surface and in the atmosphere (see below), 2) the transport
 250 by the general circulation using the “Van-Leer I” finite volume scheme from Hourdin and Armengaud (1999), 3) the
 251 mixing in the atmosphere by turbulent diffusion and possibly convection (see Section 2.5), and 4) the gravitational
 252 sedimentation of CH₄ ice particles (see below).

253 *2.8.1. Surface condensation and sublimation.*

254 The mass fluxes of methane to and from the atmosphere are computed using Eq. 8, with q_0 and q_1 the mass
 255 mixing ratios (kg/kg) just above the surface and in the middle of the atmospheric first layer, respectively. Note that
 256 an important consequence of Equation 8 is that the sublimation rate of methane is proportional to the horizontal wind
 257 velocity in the lower atmosphere.

258 When pure methane is on the surface, q_0 is set equal to the saturation vapour pressure mass mixing ratio of methane
 259 $q_{\text{sat CH}_4}$, calculated as a function of temperature T (K) and pressure p using the following expression derived from Fray
 260 and Schmitt (2009):

$$q_{\text{sat CH}_4} = 0.117 \times 10^5 e^{\frac{6.12 \times 10^5}{R} (1/90.7 - 1/T)} \times \frac{M_{\text{CH}_4}}{M_{\text{air}}} \times \frac{1}{p} \quad (14)$$

261 Here $M_{\text{CH}_4}/M_{\text{air}}$ is the ratio of molecular masses use to convert volume mixing ratio into mass mixing ratio and
 262 $R = 8.314/M_{\text{CH}_4} = 519 \text{ m}^2 \text{ s}^{-2} \text{ K}^{-1}$ the methane gas constant. When both methane and nitrogen ices are present
 263 on the surface and methane is subliming, we assume that methane is diluted in a solid solution N₂:CH₄ with 0.3%
 264 of methane (Merlin, 2015). Applying Raoult’s law, we thus set $q_0 = 0.005q_{\text{sat CH}_4}$ If the total amount of methane on
 265 the surface is sublimed within a model timestep, the flux to the atmosphere is limited accordingly. If no methane ice
 266 is present on the surface, then $q_0 = q_1$ if $q_1 < q_{\text{sat CH}_4}$ (no condensation) and $q_0 = q_{\text{sat CH}_4}$ if $q_1 > q_{\text{sat CH}_4}$ (direct
 267 condensation onto the surface). The latent heat released by methane surface condensation and sublimation is taken
 268 into account in the surface energy budget assuming a latent heat $L_{\text{CH}_4} = 5.867 \times 10^5 \text{ J kg}^{-1}$ (Fray and Schmitt, 2009).

269 2.8.2. Atmospheric condensation and CH₄ cloud formation

270 Methane can also condense (and then sublimate) in the atmosphere when the CH₄ mixing ratio exceeds the satu-
 271 ration mixing ratio provided by Equation 14. We do not know if CH₄ can easily nucleate or if large super-saturation
 272 is required. Organic particles resulting from the photochemistry in the upper atmosphere probably offer condensation
 273 nuclei suitable for heterogeneous condensation. In the GCM we assume that all atmospheric methane in excess of
 274 saturation condenses to form ice cloud particles.

275 The amount of latent heat released by methane condensation or sublimation is far from being negligible. We find
 276 that it can locally change the atmospheric temperature by more than 10 K. Moreover, latent heating actually limits the
 277 amount of methane that condenses when the atmosphere is supersaturated. If CH₄ condensation is calculated without
 278 simultaneously taking into account latent heat release, or using an explicit numerical scheme, the model predicts very
 279 unrealistic temperatures (e.g. changes larger than several tens of Kelvins within one timestep), leading to unrealistic
 280 condensation rates. In practice, at each model timestep, when the methane mass mixing ratio q_{CH_4} is detected to
 281 exceed saturation (or if methane ice is already present), one must simultaneously calculate the temperature at the
 282 end of the timestep, T' , as influenced by the condensation/sublimation and the corresponding saturation mixing ratio
 283 $q_{\text{sat CH}_4}(T')$. For this purpose we numerically determine T' by solving the following equation:

$$T' = T + [q_{\text{CH}_4} - q_{\text{sat CH}_4}(T')] \frac{L_{\text{CH}_4}}{c_p} \quad (15)$$

284 The change in CH₄ gas and ice mass mixing ratios (kg/kg) are then given by

$$\delta q_{\text{CH}_4} = -\delta q_{\text{ice}} = (q_{\text{sat CH}_4}(T') - q_{\text{CH}_4}), \quad (16)$$

285 unless all the atmospheric CH₄ ice is sublimed (and T' is adjusted accordingly).

286 Once the mass mixing ratio of CH₄ ice q_{ice} is known, the ice is distributed to form ice cloud particles around cloud
 287 condensation nuclei (CCN). We assume that the number of cloud condensation nuclei [CCN] per mass of atmosphere
 288 (kg^{-1}) is constant throughout the atmosphere. Assuming that the cloud particle size distribution is monodispersed in
 289 each volume element, the cloud particle radius r is then given by:

$$r = \left(\frac{3q_{\text{ice}}}{4\pi\rho_{\text{ice}} [\text{CCN}]} + r_{[\text{CCN}]}^3 \right)^{1/3} \quad (17)$$

290 with ρ_{ice} the CH₄ ice density (520 kg m^{-3}), and $r_{[\text{CCN}]}$ the radius of the CCN set to $0.2 \mu\text{m}$.

291 Once r is known, the cloud particle sedimentation velocity is calculated using Stokes law corrected for low pres-

sure by the Cunningham slip-flow correction (Rossow, 1978). The calculated particle radius, r , is also used to estimate the apparent opacity of the clouds. However, we neglected the radiative effect of the clouds in this paper.

[CCN] is clearly a key parameter which directly controls the properties of the clouds and their sedimentation. What is the possible range of [CCN]? On the Earth, the number mixing ratio of activated cloud condensation nuclei in the troposphere ranges between 10^6 kg^{-1} (for low saturation in clean polar air) and 10^{10} kg^{-1} (polluted air mass) [Hudson and Yun, 2002, Andreae, 2009]. It is significantly lower for icy cirrus clouds ($<10^4 \text{ kg}^{-1}$) [e.g. Demott et al. 2003]. On Pluto, it is likely that the organic haze particles may serve as CCN. In Bertrand and Forget (2016) we discuss the possible range of the mass mixing ratio for these particles. However, the actual number mixing ratio strongly depends on the degree of aggregation of the monomers and on their activation, which is poorly known. In our baseline simulations, we assumed $[\text{CCN}] = 10^5 \text{ kg}^{-1}$.

2.9. CO cycle

The CO cycle is computed using the same parameterizations than for methane, modified to use the CO properties: the CO latent heat is set to $L_{\text{CO}} = 2.74 \times 10^5 \text{ J kg}^{-1}$ and the saturation mass mixing ratio $q_{\text{sat CO}}$, is calculated as a function of temperature T (K) and pressure p (Pa) using the following expression derived from Fray and Schmitt (2009):

$$q_{\text{sat CO}} = 0.1537 \times 10^5 e^{\frac{2.74 \times 10^5}{R}(1/68.1 - 1/T)} \times \frac{M_{\text{CO}}}{M_{\text{air}}} \times \frac{1}{p} \quad (18)$$

Here $M_{\text{CO}}/M_{\text{air}}$ is the ratio of molecular masses use to convert volume mixing ratio into mass mixing ratio and $R = 8.314/M_{\text{CO}} = 296.8 \text{ m}^2 \text{ s}^{-2} \text{ K}^{-1}$ the CO gas constant.

CO is almost as volatile as N_2 and thus much more volatile than CH_4 . In practice, we found that CO only condenses when N_2 ice is present at the surface, and never forms pure CO deposits. A key parameter controlling the CO is thus the CO mixing ratio in the surface N_2 :CO ice solutions. This ratio has been estimated remotely using spectroscopic investigations of Pluto. Following the recent analysis of Very Large Telescope observations by Merlin (2015), we set this ratio to 0.3%.

3. Model initialization and choice of key parameters

Even if we had designed a perfect model of the processes at work in the Pluto environment, simulating Pluto would remain challenging. First, in spite of the New Horizons' achievements, several key parameters remain too poorly known to be used "as observed" (e.g., the global topography). Second, unlike on Mars, the Earth or even Venus, the timescales involved in the evolution of the climate system at Pluto are so long that it is difficult to reach a

319 realistic model state insensitive to the initial state, even after running the model for weeks of computer time. Here we
320 describe how we deal with these issues.

321 3.1. Topography

322 In our baseline simulations we assume a mostly flat surface except that we placed a 3800 m-deep circular crater
323 roughly at the location of Sputnik Planum (in agreement with Moore et al., 2016) as well as two smaller craters
324 corresponding to the informally-named Burney crater (1000 m deep) and Guest crater (800 m deep). See Fig. 1.

325 As discussed below, we also performed sensitivity runs with a perfectly flat topography, and with two additional
326 hypothetical 4 km-high, 800 km wide mountains that we put on the hemisphere opposite to the one better observed
327 by New Horizons (in addition to the three craters mentioned above).

328 3.2. Initial Subsurface temperatures and ices distribution on the surface

329 On Pluto, the distribution of surface ices and subsurface temperatures (which plays a key role in the Pluto environ-
330 ment) are the outcome of thousand of years of evolution (Hansen and Paige, 1996; Young, 2013; Toigo et al., 2015).
331 Running the GCM for such a long duration is not feasible. However, initializing the model with prescribed subsurface
332 temperatures and surface ice deposits unrelated to a natural surface evolution may be very unrealistic.

333 To deal with this issue, as described in Vangichith and Forget (2011) and like Toigo et al. (2015), we designed a
334 reduced version of the GCM in which the 3D atmospheric transport and dynamics are replaced by a simple global
335 mixing function for N_2 , CH_4 and CO . Such a model works well on Pluto because the surface energy balance is not
336 significantly sensitive to the atmospheric sensible heat flux and to the radiative transfer through the air. Without
337 atmospheric dynamic and complex radiative transfer to deal with, we can perform much faster numerical simulations
338 spanning more than 40,000 Earth years with the same horizontal grid, the same subsurface model, and the same
339 surface/atmosphere volatiles exchange parametrizations than with the full GCM.

340 The details of this reduced model, its validation and the results that we have obtained are described in a separate
341 paper Bertrand and Forget (2016). The key finding is that when we assume a topography map as described above
342 (Fig. 1) with a 3800 m-deep “Sputnik Planum”-like basin and a seasonal ground thermal inertia larger than 800 J m^{-3}
343 K^{-1} , after 40,000 Earth years the seasonal cycle repeats itself every year with all the nitrogen and CO ices trapped
344 in the “Sputnik Planum”-like basin. This results from the fact that nitrogen preferentially condenses at lower altitude
345 where the surface pressure is higher, inducing higher condensation temperature and thus enhanced thermal infrared
346 cooling. In this model, methane still undergoes a seasonal cycle and makes seasonal deposits in both hemispheres,
347 except in an equatorial belt which remains frost-free. Using the set of parameters described in Section 3.4 we establish
348 a realistic, equilibrated initial state for the surface N_2 , CH_4 and CO deposits and subsurface temperatures.

349 3.3. Sensitivity to initial atmospheric temperatures and winds

350 Once the surface ices and subsurface temperatures have been initialized with the reduced GCM, the full 3D GCM
 351 should be run long enough to reach a realistic regime insensitive to the initial state assumed for the atmosphere.
 352 This is challenging because of the long radiative time-scale of the Pluto atmosphere (several Earth years) and the time
 353 required to reach established methane and CO cycles in equilibrium with the surface reservoir. Sensitivity experiments
 354 performed with various initial temperatures, winds, and atmospheric CH₄ and CO contents showed that it takes about
 355 20 years for two simulations initiated with two temperature profiles chosen at the end of the realistic possibilities (e.g.
 356 differing by 30 K) to differ by less than 2 K. On this basis, we start our simulations at the end of Earth year 1988 and
 357 analyse the results after 2010. The convergences of the CO and CH₄ cycles are discussed in Section 5.

358 3.4. Two kind of simulations

359 In this paper, we describe two kinds of simulations, with and without nitrogen condensation in the south polar
 360 region in 2015.

361 3.4.1. Reference simulation, without N₂ condensation at the south pole

362 For the first simulation, we directly use the initial state obtained for Earth date 1988 after 40,000 Earth years of
 363 simulated climate history performed with the reduced model.

364 As described by Hansen and Paige (1996) and Young (2013), the evolution of pressure is sensitive to the surface
 365 N₂ ice radiative properties. Some tuning was performed to select a reference value for the N₂ ice albedo A_{N_2} and
 366 emissivity ϵ_{N_2} within the range of possible values. By choosing $A_{N_2} = 0.67$ and $\epsilon_{N_2} = 0.85$, we obtained an
 367 evolution of pressure (shown in Fig. 2) in qualitative agreement with the available observations (Sicardy et al., 2016;
 368 Gladstone et al., 2016), reaching a mean surface pressure of 1.1 Pa in July 2015.

369 Fig 1 shows the corresponding distribution of ice and subsurface temperature in 1988. In this simulation, the heat
 370 stored in the southern hemisphere during the previous southern hemisphere summer keeps the surface temperature
 371 above the nitrogen frost point, and nitrogen ice is only found in the ‘‘Sputnik Planum’’-like basin.

372 The albedo of the surface CH₄ ice deposits was set to $A_{CH_4} = 0.5$ and its emissivity to $\epsilon_{CH_4} = \epsilon_{N_2} = 0.85$.
 373 In 1988, Methane frost covers most of the planet except for an equatorial belt which remain frost free and dark (the
 374 albedo and emissivity of the ice-free surfaces were set to $A = 0.15$ and $\epsilon = 1$) in agreement with the observations
 375 (Stern et al., 2015; Grundy et al., 2016).

376 3.4.2. Alternative simulation, with N₂ condensation at the south pole

377 It is possible that nitrogen is condensing in the south polar region in 2015. In that case, we show in this paper
 378 that Pluto’s atmospheric circulation would be very different than without winter condensation, because of the induced

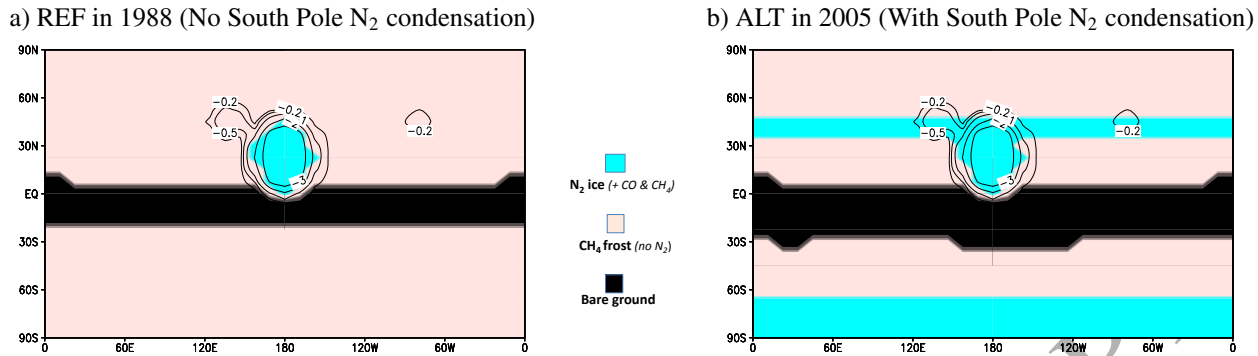


Figure 1: Maps of surface ice distribution and topography at the beginning of the reference and alternative simulations presented in this paper. The black lines show the assumed topography contours (km). **a)** : Initial state of the reference simulation with no N_2 condensation in the south polar region, in Earth year 1988. This state is the outcome of a 40,000-Earth-years simulation performed with the reduced 2D model. **b)**: Initial state of the alternative simulation with N_2 condensation in the south polar region, in Earth year 2005. This state is derived from the reference simulation state in 2005, with nitrogen added between $35^\circ N$ and $48^\circ N$ and subsurface temperature poleward of $65^\circ S$ decreased by 0.5 K.

379 North-south condensation flow. However, to be consistent with the evolution of surface pressure inferred from the
 380 stellar occultations since 1988, this winter condensation must be balanced by sublimation of nitrogen frost outside
 381 our modeled Sputnik Planum. In fact, New Horizons observations suggest that mid-northern latitude nitrogen frost
 382 deposits were present on Pluto in 2015 (Grundy et al., 2016).

383 Within that context we designed an artificial, alternative simulation by taking a modeled state from the first refer-
 384 ence simulation at the end of 2005, with two modifications. First, we added a layer of nitrogen ice in a latitudinal belt
 385 between $35^\circ N$ and $48^\circ N$. Second, we decreased the subsurface temperature poleward of $65^\circ S$ by 0.5 K to induce ni-
 386 trogen condensation. This value was chosen in order to maintain an evolution of pressure similar to the first reference
 387 run, as shown in Fig. 2. All other modeled parameters are the same as in the reference simulation.

388 4. Model results: Temperatures and winds

389 4.1. Surface temperatures and low level winds

390 4.1.1. Surface temperatures

391 Fig 3 shows maps of surface temperatures and winds at 20 m above the surface at various times of the day for
 392 our different simulations. The epoch corresponds to July 2015, the time of the New Horizons encounter. In these
 393 simulations, surface temperatures range between 36.6 and 48 K. The lowest values correspond to the N_2 frost point
 394 around 1 Pa. The highest temperatures are more model dependent, and vary with the assumed diurnal thermal inertia
 395 I_{day} . Daytime surface temperatures reach 57 K in GCM runs, assuming $I_{\text{day}} = 20 \text{ J s}^{-1/2} \text{ m}^{-2} \text{ K}^{-1}$ (as reported by
 396 Lellouch et al., 2011b) instead of $I_{\text{day}} = 50 \text{ J s}^{-1/2} \text{ m}^{-2} \text{ K}^{-1}$, as assumed in our baseline simulations.

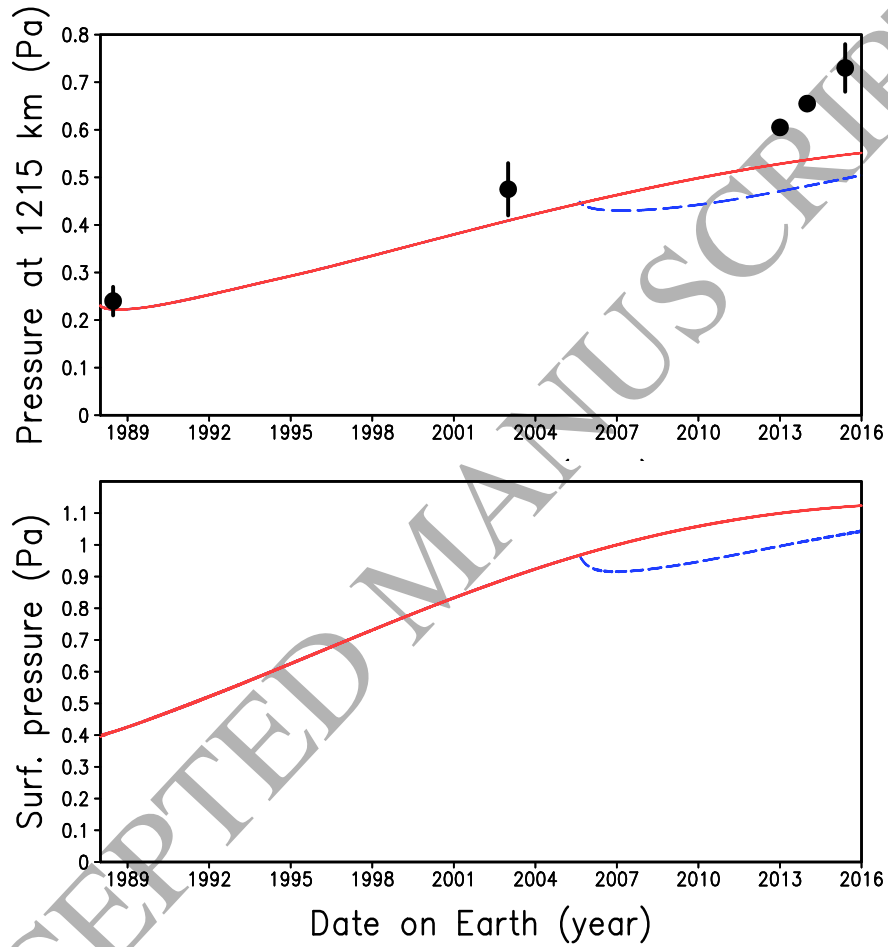


Figure 2: Evolution of the pressure at $r = 1215$ km from the planet center (**Top**) and of the global mean surface pressure (**Bottom**) in the reference simulation with no south pole N_2 condensation (red solid line) and in the alternative simulation with south pole N_2 condensation (blue dashed line) starting at the end of 2005. The black dots with error bars show the pressure data at $r = 1215$ km obtained by stellar occultations, as compiled by Sicardy et al. (2016).

397 4.1.2. Slope winds

398 On flat surfaces and where nitrogen condensation-sublimation flows are negligible, wind velocities at 20 m remain
399 well below 1 m s^{-1} . In particular surface temperature gradients do not induce significant thermal circulations. As on
400 Mars however, slopes can create significant downward katabatic winds resulting from the fact that the surface is much
401 colder than the atmosphere. The air close to the slopes is cooled and tends to flow down because it is denser than the
402 air away from the slope at the same level. Fig 4 illustrates the formation of such winds on two (hypothetical) 4-km
403 high, 800-km wide mountains. The wind at 20 m above the surface reaches 4 m s^{-1} . Because the atmosphere is always
404 warmer than the surface, and because of its long radiative timescale, the diurnal variations of surface temperature have
405 a limited effect on the katabatic winds which only increase by 20 % during the night compared to the day. Downward
406 katabatic winds can also be observed on the modeled Burney and Guest craters at 45°N in Fig 3, left column.

407 4.1.3. Surface winds induced by condensation-sublimation flows

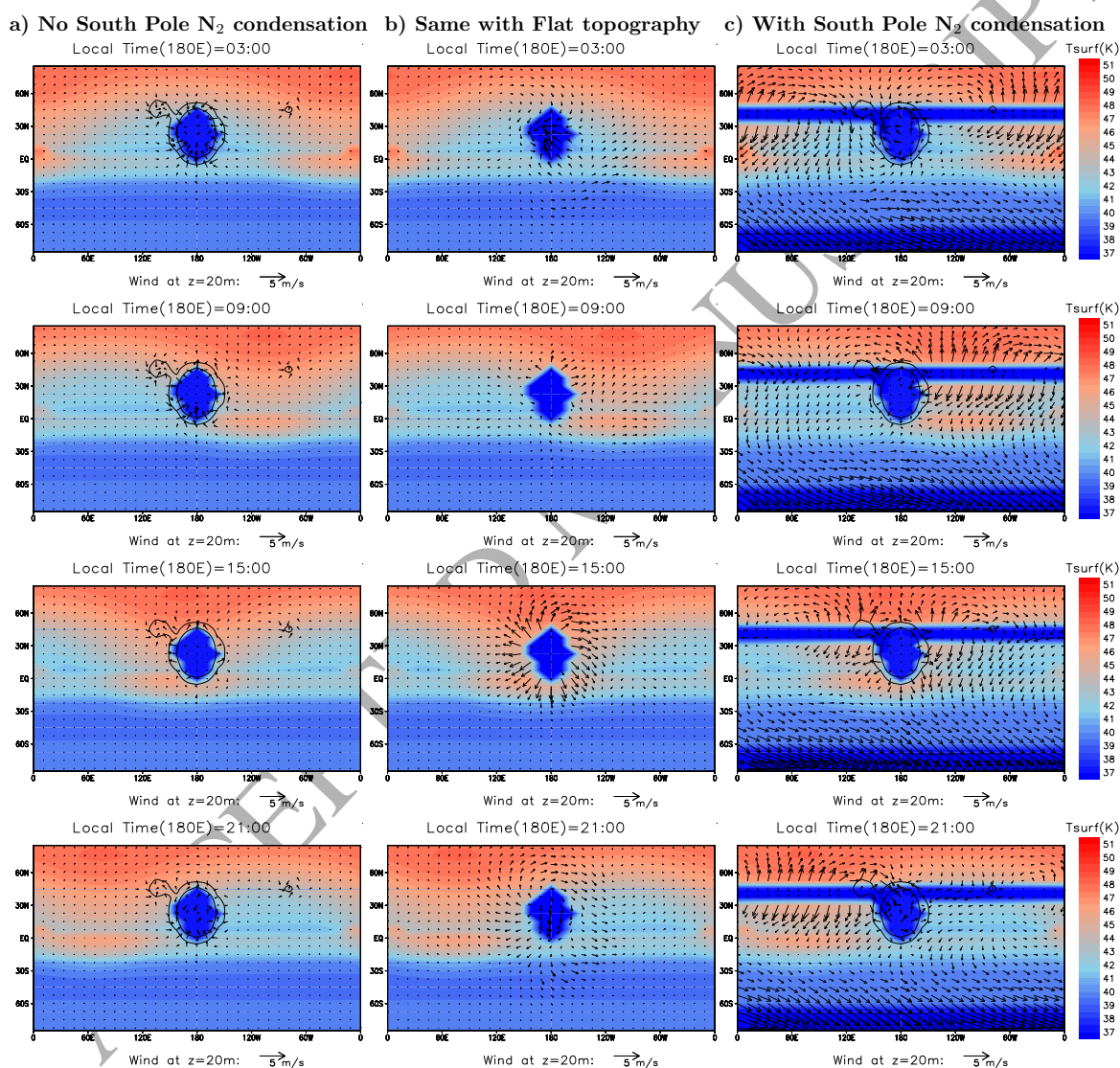
408 Wind velocities larger than several meters per second can also result from the condensation and sublimation of
409 nitrogen. In our reference circulation (with no condensation at the South pole), this only occurs in the modeled
410 “Sputnik Planum” area. If one assume a flat topography (Fig 3, center column), intense inward flows form during
411 the night when N_2 condenses, and outward flows are predicted when N_2 sublimates during the afternoon. In a more
412 realistic simulation taking into account the topographic depression in Sputnik Planum (Fig 3, left column), this effect
413 is combined with the slope winds on the sides of the basin. During the night, when N_2 condenses, both slope winds
414 and condensation flows contribute to create winds flowing into the modeled Sputnik Planum. During the day, however,
415 the outward sublimation flow is damped by the opposite katabatic flow.

416 In our alternative model (Fig 3, right column), N_2 condenses in the south polar region and this sink is balanced
417 by the sublimation of mid-northern latitude N_2 deposits. This creates planetary scale condensation flows from the
418 northern hemisphere toward the south pole, and from the dayside toward the nightside. The wind at 20 m reaches
419 several meters per seconds over most of the planet. In both hemisphere its direction is affected by the Coriolis force,
420 which prevents the atmosphere from flowing directly southward.

421 4.2. Atmospheric temperatures

422 4.2.1. Zonal-mean temperatures

423 Fig. 5 presents the zonal-mean and global-mean atmospheric temperatures. As found by Toigo et al. (2015), the
424 horizontal gradients of temperature are very small because of the long radiative timescale. In particular, the meridional
425 variations in temperatures are less than 1 K. In our reference simulation with no south pole N_2 condensation, the
426 atmospheric concentration of methane is realistic (see Section 5.1), and the mean temperature profile is in acceptable



1

Figure 3: Maps of surface temperature and winds at 20 meters above the surface in July 2015 at different local times for 3 simulations: a) the reference simulations with no N_2 condensation at the south pole, b) The same simulation with flat topography (started from the reference run on January 1st, 2015, and analyzed on July 14, 2015) c) the alternative simulation with N_2 condensation at the south pole. From top to bottom, the local time LT in the middle of the map (longitude 180°) is 3:00, 9:00, 15:00 and 21:00, with LT (hours) = $|$ longitude ($^\circ$) - subsolar point

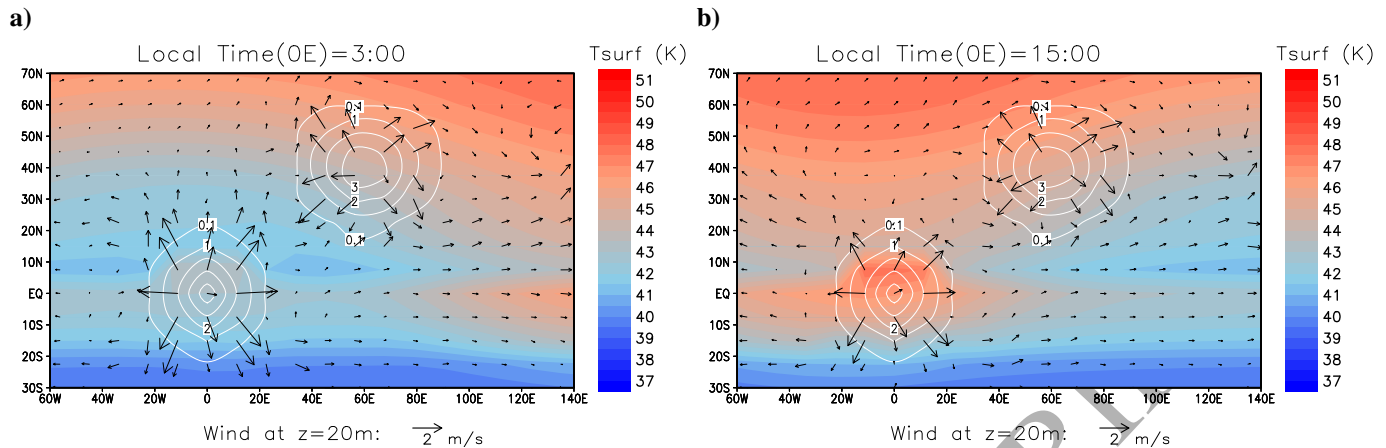


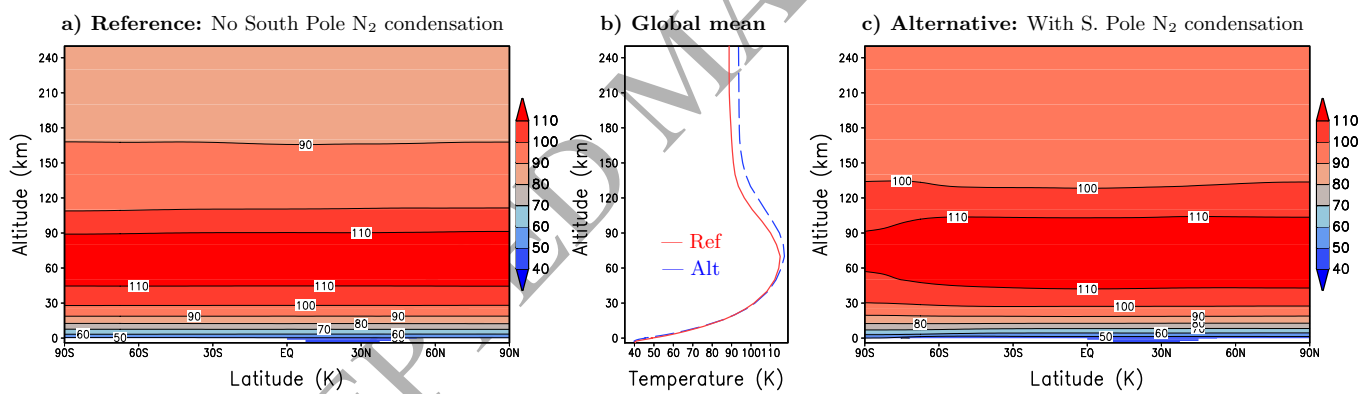
Figure 4: Maps of surface temperature and winds at 20 meters above the surface in July 2015 in the sub-charon hemisphere, where two artificial 4000 m-high mountains has been added to illustrate the formation of downward slope winds on Pluto. The topography is shown by white contours. The local time at longitude 0°E is 3:00 (nighttime) and 15:00 (daytime).

427 agreement with available observations (Hinson et al., 2015b; Gladstone et al., 2016; Dias-Oliveira et al., 2015), except
 428 that above 160 km modeled temperatures are 10 to 15 K higher than reported. The thermal structure produced
 429 in our alternative simulation with South pole N₂ condensation is even warmer, because of the excessive methane
 430 concentration in this simulation, as explained in Section 12.

431 4.2.2. Comparison with the observed REX profiles

432 In Fig. 6, the simulated temperature profiles are compared in more details with the New Horizons REX radio-
 433 occultation profiles obtained at two locations on opposite sides of Pluto. The modeled profiles are taken at the same
 434 location and time, except that the ingress profile is shifted from latitude 17.0°S to 7.5°N, in order to locate it just inside
 435 the modeled Sputnik Planum basin. Indeed, on the real Pluto the ingress profile corresponds to a location just above
 436 the southern tip of the Sputnik Planum depression, above a surface covered by nitrogen ice. At the same coordinates
 437 in our model, we are outside the basin and the surface is frost free. However, we found that taking into account the low
 438 topography and N₂ coverage is key to understand the differences between the two REX profiles. We plot the modeled
 439 temperature profiles as a function of altitude above the surface. This creates an apparent shift in temperatures (the
 440 profiles are much more similar when shown in pressure coordinates) which contributes to the apparent differences
 441 reported in the observations.

442 Of special interest are the lowest kilometers of the simulated ingress profiles which exhibit a low temperature layer
 443 analogous to the bottom of the observed ingress profile. Which process creates this layer? To better understand this
 444 behaviour, and possibly interpret the observations, we show in Fig 7 the diurnal evolution of the atmospheric profile
 445 in the lowest 4 km in different modeled configurations. In the reference simulation, the atmospheric temperature in



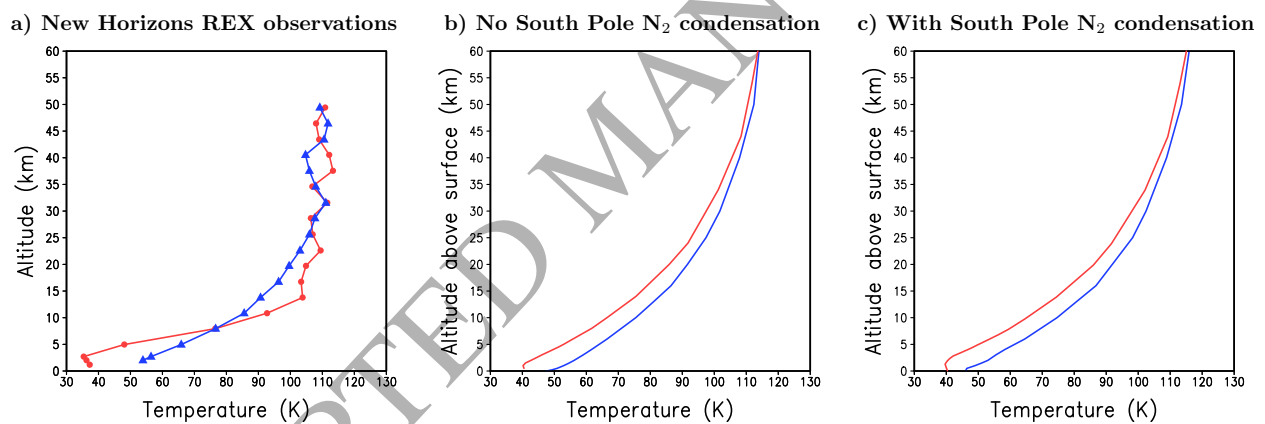
446 the Sputnik Planum basin varies with local time, with coldest temperatures in the afternoon. This results from the
 447 sublimation of nitrogen ice when the sun heats the area, as proposed by Hinson et al. (2015a). In fact, the volume of
 448 gas involved in the condensation-sublimation cycle is considerable in our model. Fig. 8 shows the nitrogen ice budget
 449 in the modeled Sputnik Planum basin at 7.5°N and 45°N . At this last position, about 230 g m^{-2} of ice sublimates
 450 every Pluto day in 2015. As shown on the right axis of Fig. 8, this corresponds to more than 2500 m^3 of N_2 gas per
 451 square meter. At 7.5°N , the solar flux is weaker in 2015 and the daily N_2 ice budget corresponds to a net gain in N_2
 452 ice (net condensation). Nevertheless, every afternoon the equivalent of 800 m^3 per square meters is injected into the
 453 atmosphere. Moreover, in the GCM the large amount of cold N_2 gas produced at higher latitude (where the insolation
 454 is higher) is spread throughout the basin in the lowest kilometers. In fact, in the alternative simulation this process
 455 contributes to increasing the amount of cold air present in the modeled Sputnik Planum basin (Fig. 7b), adding the
 456 freshly-sublimed cold N_2 gas transported from the N_2 ice belt at 35°N (as seen on Fig. 3, right column, local time
 457 15:00 and 21:00).

458 Interestingly, as shown in Fig. 7c, a simulation performed without taking into account the topographic depression
 459 in the modeled Sputnik-planum does not create a significant cold layer. Two facts explain that. First, the freshly-
 460 sublimed N_2 gas is efficiently transported away as discussed above (and as seen on Fig. 3, mid-column). Second,
 461 in an atmosphere with radiative timescale as long as Pluto, in a local topographic depression the temperature lapse
 462 rate is not as steep as on average because temperatures tend to be homogeneous at a given pressure level. This is
 463 illustrated on Fig. 7d which shows the temperatures at the bottom of the basin in a simulation with N_2 condensation
 464 and sublimation completely switched off. Without N_2 sublimation, the air is not as cold as in the reference simulation,
 465 but at a given altitude above the surface, temperatures in the basin remain 5 to 10 K below what they would have been
 466 outside (compare Fig. 7c and Fig 7d).

467 4.2.3. Thermal tides and waves

468 Stellar occultations have shown that vertical profiles of density fluctuations in the atmosphere of Pluto often
 469 exhibit wave-like structure (e.g. Elliot et al., 2003b; Person et al., 2008) with an amplitude of a few percent and
 470 vertical wavelengths of a few kilometers. On the basis of theoretical calculations, Toigo et al. (2010) suggested that
 471 such waves could correspond to the tidal response of Plutos atmosphere to solar-induced sublimation breathing from
 472 N_2 frost patches. Here we briefly examine the type of wavelike structure present in the temperature profiles generated
 473 by our GCM. Note, however, that the horizontal and vertical resolution used in the GCM simulations is unlikely to
 474 capture waves with vertical wavelengths smaller than $\sim 20\text{ km}$.

475 Fig. 9a presents the 4-sols evolution of the difference between instantaneous temperatures and 1-Pluto-day gliding
 476 averages at $0^{\circ}\text{E} - 0^{\circ}\text{N}$ in our reference simulation. The observed temperature excursions are lower than 0.2 K. Nev-



1

Figure 6: Comparison of the two temperature profiles retrieved by the New Horizons REX experiment (Hinson et al., 2015b; Gladstone et al., 2016) at 193.5°E , 17.0°S and Local time 16:31 (**red**) and 15.7°E , 15.1°N and Local time 04:42 (**blue**) with GCM results. The model data are taken at the same location and time, except for the profile at latitude 17.0°S which is shifted to 7.5°N in order to locate it just within the modeled Sputnik Planum basin filled with N_2 ice, as it is the case in reality (see text).

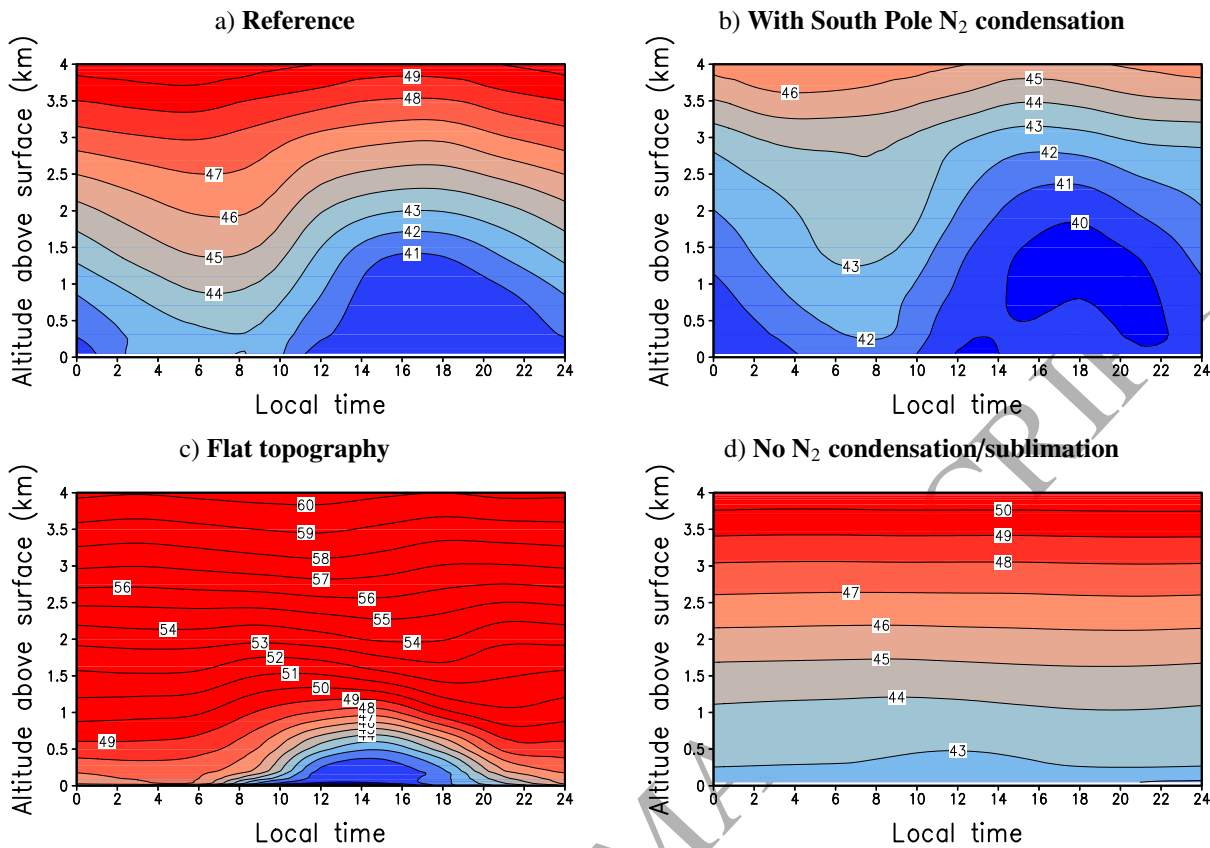


Figure 7: Diurnal variations of atmospheric temperature in the lower atmosphere at $193.5^{\circ}\text{E}-7.5^{\circ}\text{N}$ (at the bottom of the modeled Sputnik Planum basin) for (a) the reference simulation (without South Pole N_2 condensation), (b) the alternative simulation (with South Pole N_2 condensation), (c) a version of the reference simulation with a flat topography, and (d) No N_2 condensation/sublimation at all on the planet. The simulations with flat topography and No N_2 condensation/sublimation were started from the reference run initial state on January 1st, 2015, and analyzed on July 14, 2015.

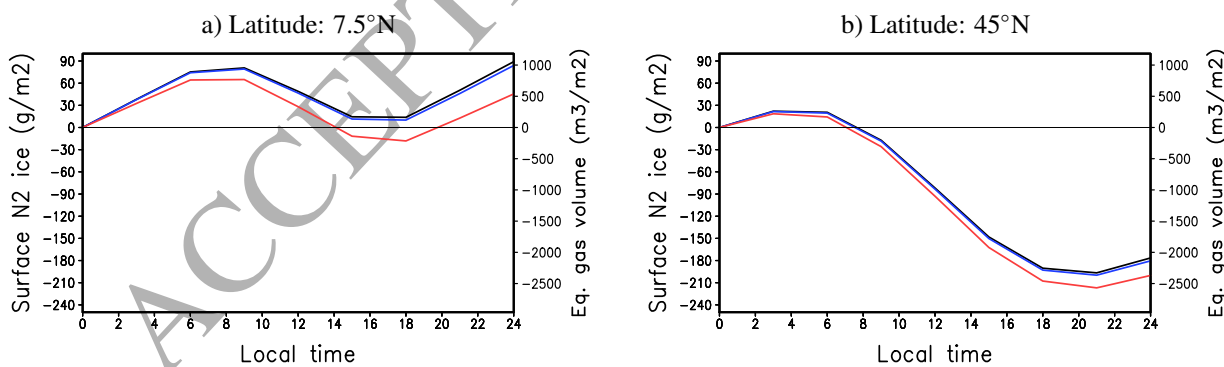


Figure 8: Diurnal variation of the surface N_2 ice loading at two different latitudes in the modeled “Sputnik Planum” basin in July 2015. The right axis illustrates the corresponding volume of N_2 gas, assuming a pressure of 1 Pa and a temperature of 40 K. The different line colours correspond to different kinds of simulations: reference (blue), alternative with South pole N_2 condensation (black, partly hidden by the blue line), and with a flat topography (red). The curves do not loop (i.e. the values at 24:00 differ from the values at 0:00) because every Pluto day the integrated surface budget corresponds to a net gain of N_2 ice by condensation at 7.5°N and a net loss by sublimation at 45°N , where the incident solar flux is stronger than at 7.5°N .

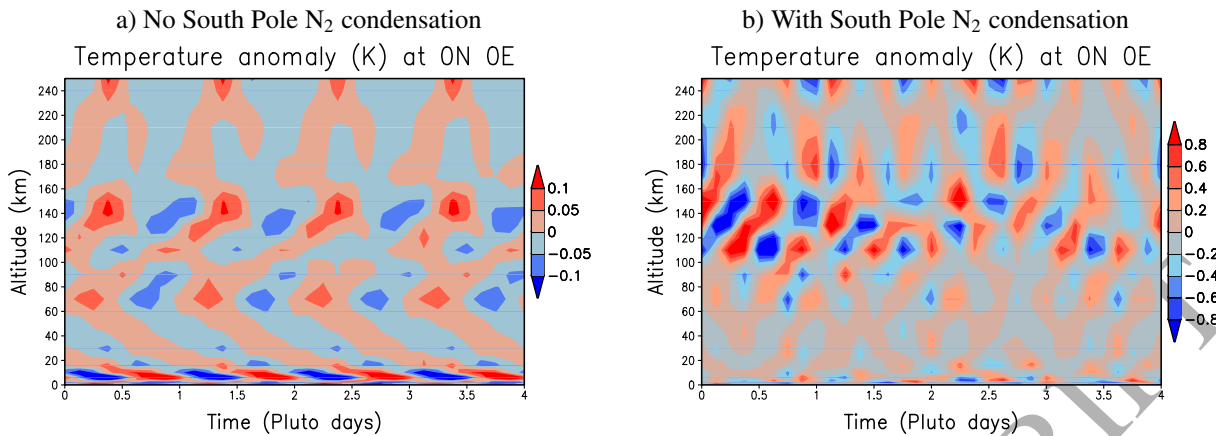


Figure 9: Temperature anomaly (difference between instantaneous value and diurnal average) at $0^{\circ}\text{E} - 0^{\circ}\text{N}$ in the reference and alternative simulations in July 2015. Thermal tides are clearly visible in the reference simulation, whereas the alternative simulation is characterized by atmospheric barotropic waves (see text).

477 ertheless, they are characteristic of upward atmospheric thermal tides, with, below 80 km, diurnal, wavenumber=1
 478 thermal tides with a vertical wavelength around 20 km and a downward phase velocity. Above 150 km, semi-diurnal
 479 wavenumber=2 tide with much longer vertical wavelengths start to dominate. As predicted by Toigo et al. (2010), the
 480 source of the tides is the diurnal N_2 condensation-sublimation cycle of the N_2 ice: Tidal amplitude are 4-times weaker
 481 if N_2 condensation-sublimation processes are switched off.

482 Fig. 9b presents the same anomaly plot in the alternative simulations with N_2 condensation occurring at the south
 483 pole. The amplitude of the waves are significantly larger, reaching more than ± 1 K around 120 km. However, a careful
 484 examination of Fig. 9b reveals that the period of the stronger waves is not 1 nor 0.5 Pluto day. These are not thermal
 485 tides: the same waves are present in simulations forced by a diurnally-averaged insolation (no diurnal cycle and no
 486 tides). These waves appear to be barotropic waves produced by a southern polar jet, as described in Section 4.3.2.

487 4.3. Atmospheric circulation and waves

488 Fig. 10 shows cross-sections of the average zonal (west-east) and meridional (south-north) winds in our two
 489 baseline simulations.

490 4.3.1. Reference Case without N_2 condensation at the south pole,

491 In the reference case with no condensation-flow induced by N_2 condensation at the south pole, the circulation is
 492 relatively weak with slow retrograde zonal winds in the northern hemisphere and the equatorial regions (Fig. 10a).
 493 This circulation remains unchanged with a flat topography, no diurnal cycle, or when N_2 condensation and sublimation
 494 processes are switched off. It can be explained by the north-south latitudinal gradient of solar heating rates. It induces
 495 a very small temperature contrast between the spring and fall hemisphere and, in turn, forces weak zonal winds

496 corresponding to the thermal wind balance. Consistently, the weak meridional circulation (Fig. 10c) is characterized
497 by a cell centered at the equator (where the Coriolis force is null) between 80 and 140 km, with the upper branch
498 flowing from the sunlit hemisphere toward the polar night hemisphere.

499 4.3.2. *Alternative case with N₂ condensation at the south pole,*

500 The circulation is profoundly influenced by the North-South condensation flow if N₂ condenses in the South polar
501 regions.

502 If N₂ ice deposits were covering the entire northern polar regions (which is not observed) and the southern hemi-
503 sphere condensation much more intense, the condensation flow would be very strong. As obtained in some of our
504 past simulations (not shown) and as reported in some scenarios analysed by Toigo et al. (2015) (see their Fig. 11
505 and 18), the meridional circulation would be characterized by a global flow from the northern hemisphere to the
506 southern hemisphere. In such conditions, the zonal circulation is characterized by a global “retro-superrotation” with
507 retrograde winds at most latitude. Such winds result from the conservation of angular momentum of the air particles
508 as they flow from the sunlit pole to the polar night above the equator, where they are farther from the rotation axis
509 than where they started from.

510 In our simulations however, the North-South condensation flow remains limited compared to this extreme case.
511 We consider that this is in better agreement with the observations because 1) outside Sputnik Planum the N₂ ice frost
512 deposits are limited to patches around 45-60°N (Grundy et al., 2016), and 2) because the south pole N₂ condensation
513 cannot be very intense in 2015 since Pluto’s surface pressure has been increasing in recent years.

514 With the realistic assumptions made in our “alternative” simulation, the meridional circulation remains weak
515 (Fig. 10d) and strongly modulated by waves (see below). The overall transport pattern is southward, as revealed when
516 analysing tracer transport (Bertrand and Forget, 2016).

517 The zonal wind is characterized by an intense prograde jet-stream poleward of 40°S and a prograde superrotation
518 at most other latitudes (Fig. 10c). The high-latitude jet is a classical feature of terrestrial atmospheres, and likely
519 result here from the poleward condensation flow and the conservation of angular momentum. Superrotation is more
520 surprising. It is observed on Venus and Titan and has been the subject of many studies (see, e.g. Lebonnois et al., 2010,
521 and references therein). In these cases, superrotation is considered to primarily result from the so-called Gierasch-
522 Rossow-Williams mechanism (from Gierasch, 1975; Rossow, 1979). In this mechanism, waves, possibly generated by
523 barotropic instabilities from the high-latitude jets, redistribute angular momentum equatorward. Preliminary analysis
524 suggest that this is what is happening in our simulation. A study of the variations of the high-latitude jet show that it is
525 subject to instabilities that create a wavenumber 1 wave that propagates eastward with a 0.5-0.8 Pluto day period. At
526 60°N, such waves are clearly visible at an altitude of 140 km in the temperature and meridional wind fields (Fig. 11b

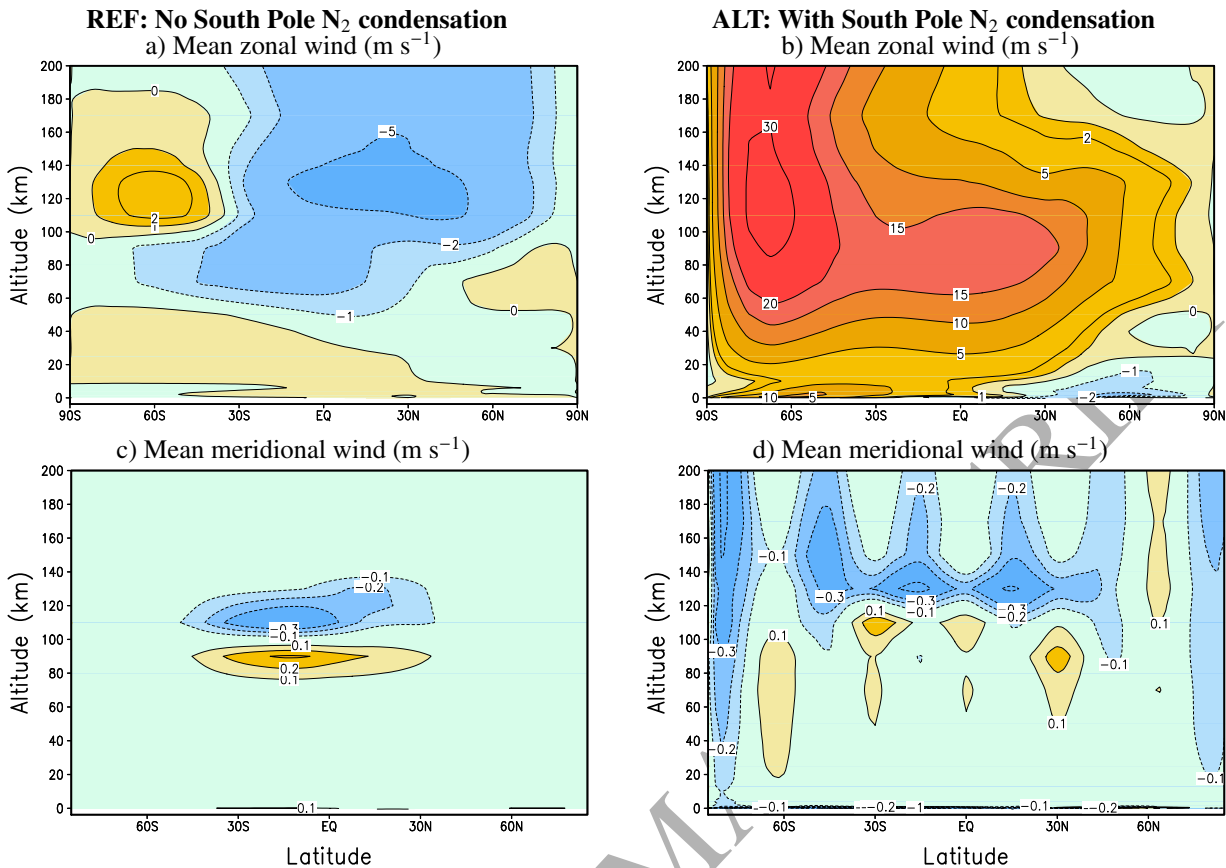


Figure 10: Zonal-mean zonal and meridional winds (m s^{-1}) in the reference and alternative simulations in July 2015.

527 and 11d). In Fig. 11c, the extension of this wave is mapped by plotting the meridional wind variability as a function
 528 of latitude and height. One can see that it propagates to all latitudes, and notably to the equator, where the signature in
 529 the thermal field dominates the temperature variability (Fig. 11a). Similar results are obtained in model runs without
 530 a diurnal cycle or with a flat topography.

531 In addition to the wind predictions published by Toigo et al. (2015), already discussed, our results can be compared
 532 with the results from the other Pluto GCM proposed by Zalucha and Michaels (2013) and Zalucha (2016). The
 533 comparison with Zalucha and Michaels (2013) is difficult to achieve because this version of their GCM did not yet
 534 include nitrogen condensation and because their modeled thermal structure was very different than what was observed
 535 on Pluto by New Horizons. In fact the updated version presented by Zalucha (2016) yielded completely different
 536 results. Her “Case 1”, in which a surface pressure of 0.8 Pa and 1% of CH_4 is assumed, can be compared to our
 537 simulations. The zonal wind structure resemble our reference simulation, suggesting that, for unknown reasons, the
 538 condensation flow is weak in this GCM in spite of the fact that Pluto is assumed to be covered by nitrogen ice.

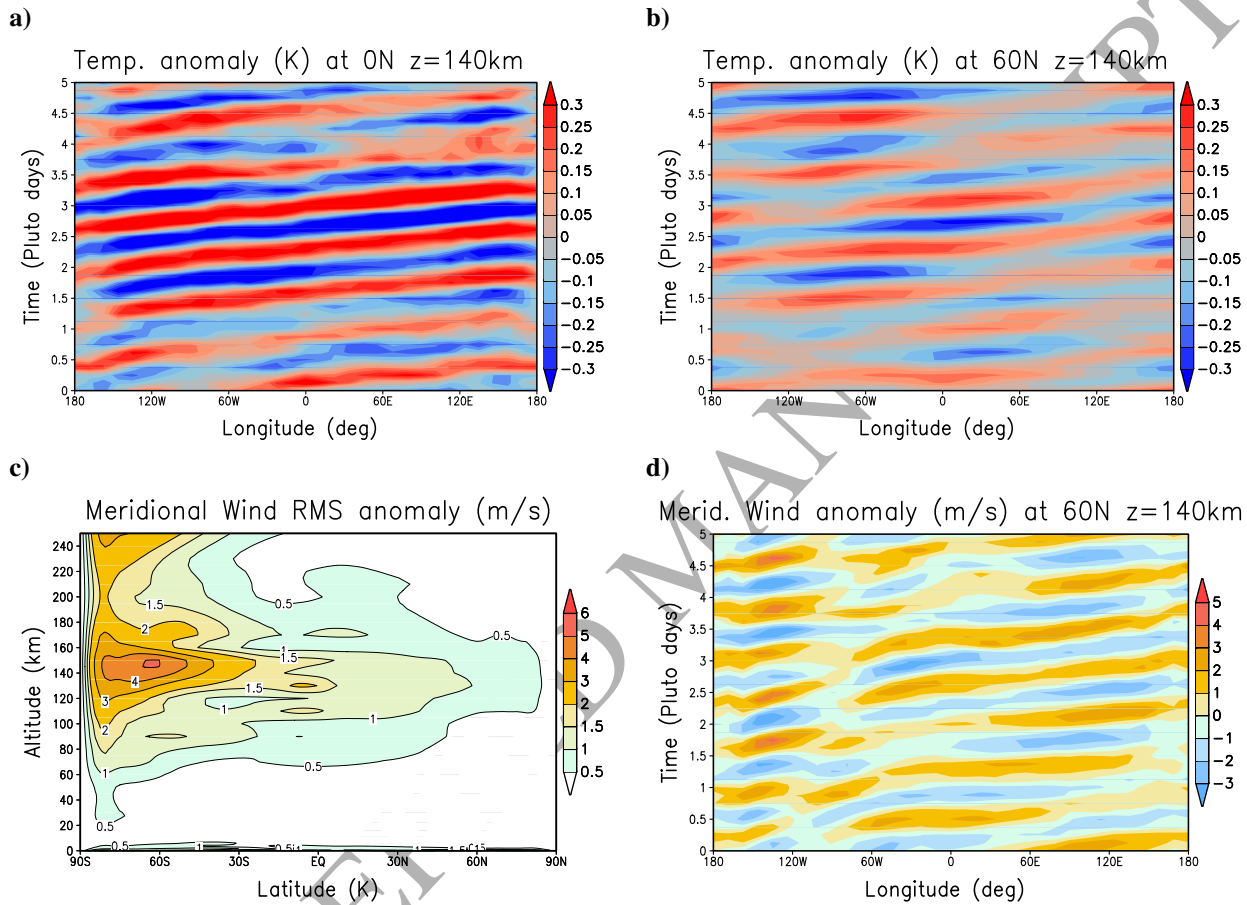


Figure 11: Characteristics of the barotropic waves present in the simulations with South Pole N_2 condensation inducing a condensation flow. **a)** Hövmoller diagram of the temperature anomaly (difference between the local and the zonal-mean temperature) at $0^\circ N$. **b)** Same at $60^\circ N$. **c)** Zonal average of the root-mean-square standard deviation of the local meridional wind from the zonal-averaged meridional wind. **d)** Hövmoller diagram of the meridional wind anomaly (difference between the local and the zonal-mean wind, in $m s^{-1}$) at $0^\circ N$.

5. Model results: CH₄ and CO cycles

5.1. Evolution and distribution of gaseous CH₄

Fig. 12 shows the global-mean mixing ratio of methane (determined from the ratio of CH₄ and N₂ column densities) in our baseline simulations, and how this ratio varies over time. Fig. 12c shows the evolution of the global-mean mixing ratio of methane. The three red curves correspond to reference simulations (without poleward condensation flow) with methane volume mixing ratio initialized at 0.1%, 0.5% and 1% in 1988. One can see that in 2015 the results are still sensitive to the initialization, although the three simulations clearly converge toward a global mean value near 0.5%. Fig. 12a and b present the zonal-mean methane abundances as a function of latitude and altitude in 2010 (mid-point between the 2008 and 2012 observations by Lellouch et al., 2015) and 2015 (New Horizons). These figures show that methane is not homogeneously distributed, notably because the high latitude deposits are increasingly heated and sublimed as the sub-solar point moves northward with time. As a result methane tends to be enriched in the lower atmosphere at high northern latitudes compared to the rest of the planet, but is otherwise vertically well mixed and near 0.5% at most altitudes. This is consistent with the observation analysis of Lellouch et al. (2015) who concluded that their data “imply a roughly uniform mixing ratio in at least the first 22–27 km of the atmosphere”, and that “high concentrations of low-temperature methane near the surface can be ruled out”. To compare with Earth-based near-infrared observations, one must nevertheless take into account the fact that such observations are biased toward the methane column near the sub-Earth-subsolar points for geometrical reason (Pluto is a sphere) and because this is where the insolation is maximum. Taking into account that the sub-Earth and subsolar points are always very close, we can estimate the apparent mixing ratio as seen from the Earth by performing an average of the local column mixing ratio weighted by the square of the cosine of the solar zenith angle. The apparent mixing ratio for the reference simulations started with 0.5% CH₄ is shown in green on Fig. 12c. The difference with the global-mean value remain small and has only become significant recently with the local increase of methane above the North pole.

On the same Figure 12c, the blue dashed curve shows the evolution of the global-mean methane in the alternative scenario (with N₂ condensing at the south pole) starting in 2005. Fig. 12d show the corresponding methane abundances as a function of latitude and altitude in 2015. One can see that the methane content is larger and still increasing in this simulation. This results from the stronger near-surface winds induced by the condensation flow, and the fact that the near-surface mixing is directly proportional to the horizontal wind as formalized in Equation 8 presented in Section 2.5.

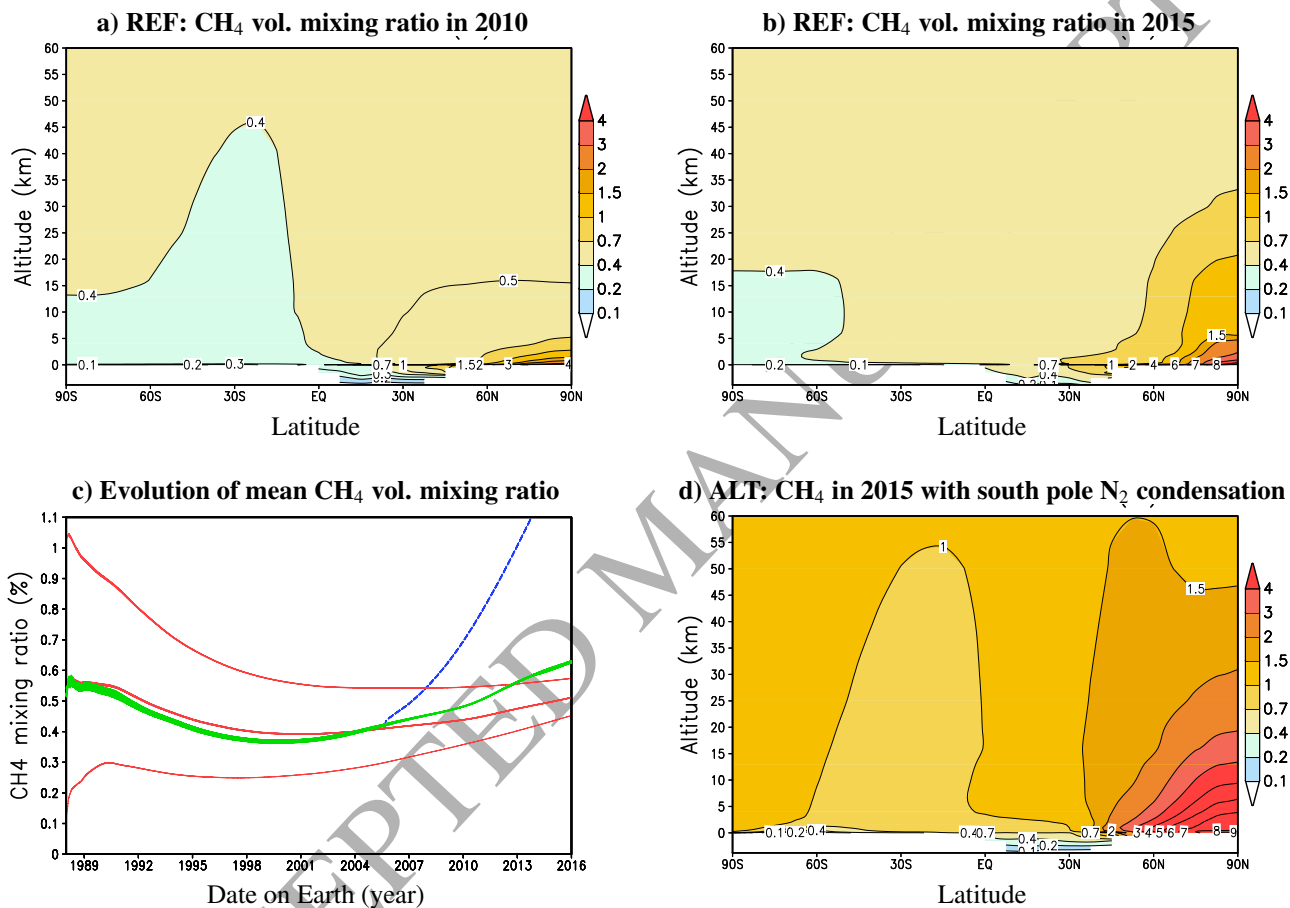


Figure 12: **a) - b):** Zonal mean methane volume mixing ratio (%) in the reference simulation (without south pole N₂ condensation and [CH₄] initially at 0.5% in 1988) in 2010 and 2015. **c):** Evolution of the mean volume mixing ratio: globally averaged with different initialization (red), the apparent mixing ratio as seen from the Earth (green, see text) and in the alternative simulation with south pole N₂ condensation started in 2005 (dashed blue). **d):** Zonal mean methane volume mixing ratio (%) in the alternative simulation (with south pole N₂ condensation) in 2015.

567 5.2. Formation of CH₄ ice clouds

568 Fig 13 shows maps of methane ice clouds in our reference and alternative simulations at various local time in July
 569 2015. In both simulations, atmospheric condensation is induced by the subliming nitrogen ice on the surface. On the
 570 dayside, freshly-sublimed nitrogen gas tends to cool the atmosphere nearby and trigger methane condensation in the
 571 first hundreds of meters above the surface, as illustrated in Fig 14. In the alternative simulations with surface N₂ ice
 572 between 35°N and 48°N, the cold air and the clouds particles are transported by the sublimation flows (see Fig 3, right
 573 column) and can extend outside the N₂ ice covered regions, reaching 20°N and 75°N.

574 5.3. CO cycle

575 Fig. 15 shows the evolution of the carbon monoxide mixing ratio as a function of time since 1988. The red curves
 576 correspond to the global-averaged mixing ratio for three different initial values (0%, 0.05%, 0.1%). Clearly, the three
 577 simulations have not converged but one can estimate that the system evolves toward a mean mixing ratio near 0.03%.
 578 A mixing ratio of 0.03% is in acceptable agreement with the $0.05^{+0.01}_{-0.025}\%$ reported by Lellouch et al. (2011a) from
 579 telescopic observations performed in 2010, and of the same order of magnitude as the $0.0515 \pm 0.004\%$ just retrieved
 580 by Lellouch et al. (2016) using the ALMA interferometer on June 12-13, 2015.

581 In details, the CO cycle is dominated by a condensation-sublimation cycle inside Sputnik Planum. For instance
 582 in 2015 there is a net flux from the northern part and the center part of Sputnik Planum to the southern part where
 583 nitrogen is condensing along with CO. We do not show here the spatial distribution of CO since we have found that
 584 CO is usually very well mixed with N₂. As a consequence, the apparent CO mixing ratio as seen from the Earth (green
 585 curve in Figure 15) is very close to the global mean.

586 When the alternative simulation is started in 2005 with N₂ condensing in the high southern latitudes (blue lines
 587 in Figure 15), the CO mixing ratio rapidly decreases to reach values below 0.03%. This is even the case when we
 588 assume that all mid-northern latitude N₂ frost deposits contains 0.3% of CO. In these conditions, the atmospheric CO
 589 appears to decrease below 0.03% because the ices that condense in the south polar cap tends to be enriched in CO, up
 590 to 0.05% at the pole.

591 In reality, the mid-latitude N₂ frost deposits have been observed by New Horizons to be strongly depleted of CO
 592 compared to Sputnik Planum (Grundy et al., 2016). If we take this into account and set the N₂:CO mixing ratio to
 593 zero in these deposits, we obtain the evolution shown by the dashed blue line Figure 15, with an additional decrease of
 594 atmospheric CO down to less than 0.01% in 2015. One can guess that these values could be tuned up by increasing the
 595 assumed N₂:CO ice mixing ratio in Sputnik Planum. This would still be consistent with the Merlin (2015)'s telescopic
 596 measurements since they included both Sputnik Planum and the mid-latitude deposits. Further work will be required
 597 to fully understand the long term CO equilibrium, its evolution, and the surface N₂:CO mixing ratio.

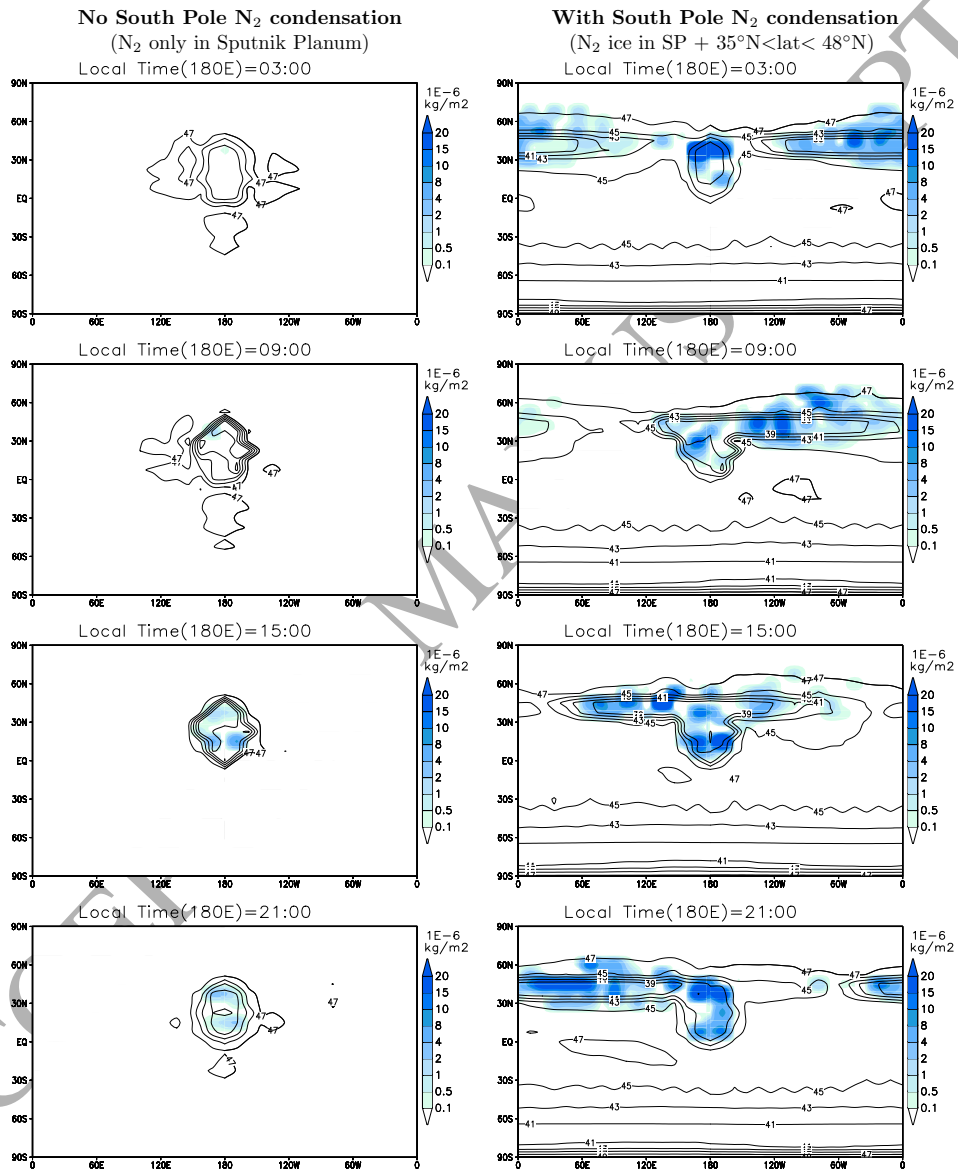


Figure 13: Maps of methane ice clouds mass (10^{-6} kg per m^2) in July 2015 for the reference and alternative simulations for different local times at center of the map (180° E). The black contours show the atmospheric temperature 20 m above the surface.

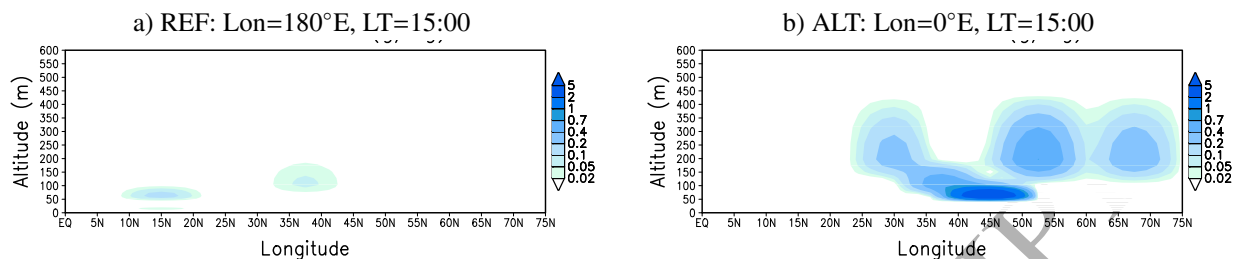


Figure 14: Methane clouds as a function of latitude and altitude above the surface, around July 14 2015, in a) the reference simulation (N_2 only in Sputnik Planum) at longitude $180^\circ E$ and Local Time 15:00, and b) the alternative simulation (with surface N_2 ice between $35^\circ N$ and $48^\circ N$) at longitude $0^\circ E$ and Local Time 15:00.

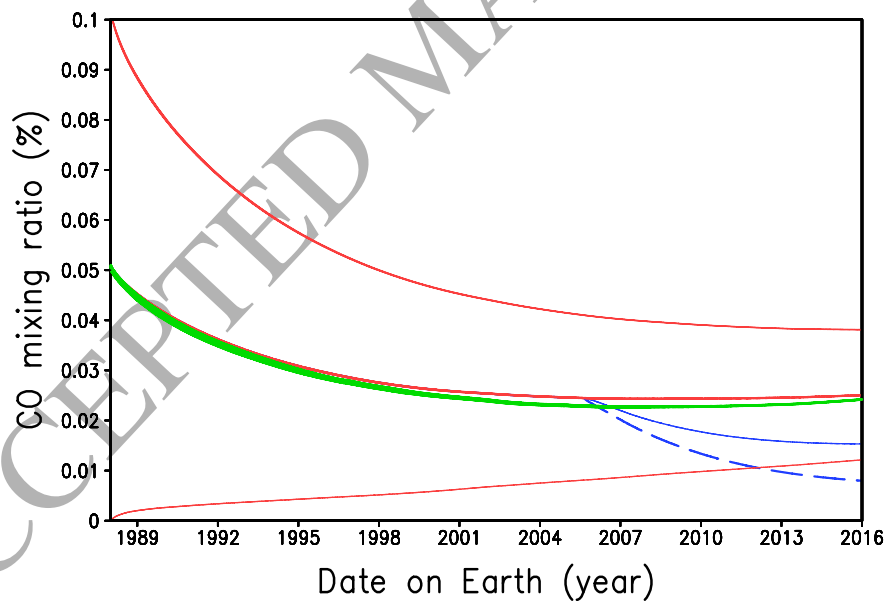


Figure 15: Evolution of the mean volume mixing ratio of gaseous carbon monoxide. The red curves present the globally averaged values with different initialization. The green curve shows the apparent mixing ratio as seen from the Earth. The blue curves shows the global mean mixing ratio in the alternative simulation with south pole N_2 condensation started in 2005 (see text).

598 5.4. Conclusions

599 The goal of this paper was to describe, for the first time, our new Global Climate Model of Pluto including the
600 N_2 , CH_4 and CO cycles. We presented two baseline simulations which can shed light on New Horizons observations,
601 for instance to understand the low atmosphere temperature profiles measured by REX and the distribution of ices.
602 However, this is just the beginning. One of our key conclusions is that the Pluto climate system is extremely sensitive
603 to the assumed model parameters, such as the ice properties, the ground thermal inertia, or the topography. Many
604 more studies will have to be performed to better simulate the reality and understand the processes at work. It will
605 also be very useful to perform longer simulations, with higher model resolution, with a more realistic topography,
606 etc... We hope that this GCM will be applied to many specific studies regarding clouds, hazes, frost deposits, seasonal
607 evolution, and paleoclimates.

608 **APPENDIX: Computing mass, momentum and heat vertical fluxes induced by N_2 condensation and sublima-**
609 **tion in the GCM vertical coordinates**

610 In the GCM, the changes in atmospheric mass due to the condensation and sublimation of nitrogen are taken
611 into account by modifying the surface pressure p_0 at each timestep by: $\delta p_0 = -g \sum_{k=0}^N \delta m_k$, with N the number of
612 atmospheric model layers and δm_k the mass condensed (or sublimed if < 0) in layer k or at the surface ($k = 0$), as
613 described in Section 2.6. This ensures the conservation of the total mass of N_2 (surface caps + atmosphere).

614 As described in Section 2.1, the vertical coordinate of each model layer is defined by its $\sigma_l = p_l/p_0$ coordi-
615 nates. The changes in p_0 due to the N_2 condensation-sublimation induce “artificial” movements of the σ levels in the
616 atmosphere. This must be reflected in the temperature and wind fields.

617 Consider a layer l delimited by the levels $\sigma_{l-\frac{1}{2}}$ and $\sigma_{l+\frac{1}{2}}$. At each timestep, its mass $M_l = \frac{p_0}{g}(\sigma_{l-\frac{1}{2}} - \sigma_{l+\frac{1}{2}})$ (in
618 $kg\ m^{-2}$) varies because of the global variation of p_0 . Such a variation δM_l is associated with transfers of mass between
619 the layers (on which one must add the sink corresponding to the local condensation $-\delta m_l$). The local mass balance
620 may be written :

$$\delta M_l = \frac{\delta p_0}{g}(\sigma_{l-\frac{1}{2}} - \sigma_{l+\frac{1}{2}}) = W_{l-\frac{1}{2}} - W_{l+\frac{1}{2}} - \delta m_l \quad (19)$$

621 where $W_{l-\frac{1}{2}}$ is the air mass ($kg\ m^{-2}$) “transferred” through the level $\sigma_{l-\frac{1}{2}}$ (> 0 when up) during the timestep. Equa-
622 tions 19 can be rearranged to yield a recursive formula on W :

$$W_{l+\frac{1}{2}} = W_{l-\frac{1}{2}} - \delta m_l - \frac{\delta p_0}{g}(\sigma_{l-\frac{1}{2}} - \sigma_{l+\frac{1}{2}}) \quad (20)$$

623 with, in the first layer:

$$W_{\frac{1}{2}} = -\delta m_0 \quad (21)$$

624 The knowledge of W can then be used to compute the exchange of heat and momentum between the layers. For
625 $c_p T$ (enthalpy), the local heat balance can be written :

$$\delta(M_l T_l) = W_{l-\frac{1}{2}} \bar{T}_{l-\frac{1}{2}} - W_{l+\frac{1}{2}} \bar{T}_{l+\frac{1}{2}} - \delta m_l T_{c_l} \quad (22)$$

626 with $\bar{T}_{l-\frac{1}{2}}$ the mean temperature of the gas transported through the $\sigma_{l-\frac{1}{2}}$ interface. The calculation of $\bar{T}_{l-\frac{1}{2}}$ is like
627 in a classical transport problem. We use the ‘‘Van-Leer I’’ finite volume transport scheme (Van Leer, 1977; Hourdin
628 and Armengaud, 1999). Separately, one can also write :

$$\delta(M_l T_l) = (M_l + \delta M_l) \delta T_l + T_l \delta M_l \quad (23)$$

629 with δT_l the correction to be applied at every timestep in each layer after the N_2 condensation or sublimation.
630 Eqs 22 and 23 may be combined to obtain δT_l

$$\delta T_l = \frac{1}{M_l + \delta M_l} [W_{l-\frac{1}{2}} (\bar{T}_{l-\frac{1}{2}} - T_l) - W_{l+\frac{1}{2}} (\bar{T}_{l+\frac{1}{2}} - T_l) - \delta m_l (T_{c_l} - T_l)] \quad (24)$$

631 The first two terms, with $W_{l-\frac{1}{2}}$ and $W_{l+\frac{1}{2}}$, correspond to the re-arrangement of the temperatures over the entire
632 column due to the pressure variations in σ coordinates. The last term $\delta m_l (T_{c_l} - T_l)$ is negligible when N_2 condenses
633 or partially sublimates since we then have $T_{c_l} = T_l$. However, when the N_2 totally sublimates, it becomes a cooling term
634 accounting for the mixing of the newly sublimed mass $-\delta m_l$ with the rest of the layer at $T_l > T_{c_l}$.

635 On the ground, if $\delta m_0 > 0$ (condensation), we set $\bar{T}_{\frac{1}{2}} = T_1$. As mentioned above, the near-surface cooling of the
636 condensing N_2 gas from T_1 to T_0 is then taken into account in the surface energy balance. If $\delta m_0 < 0$ (sublimation),
637 we set $\bar{T}_{\frac{1}{2}} = T_0$. The term $\delta m_0 (T_0 - T_1)$ then accounts for the cooling of the lowest level by the freshly-sublimed
638 nitrogen.

639 Similarly, the momentum distribution must be re-arranged. For a wind component v , we shall simply write:

$$\delta v_l = \frac{1}{M_l} [W_{l-\frac{1}{2}} (\bar{v}_{l-\frac{1}{2}} - v_l) - W_{l+\frac{1}{2}} (\bar{v}_{l+\frac{1}{2}} - v_l)] \quad (25)$$

640 with, on the ground, $\bar{v}_{\frac{1}{2}} = v_1$ if $\delta m_0 > 0$ and $\bar{v}_{\frac{1}{2}} = 0$ if $\delta m_0 < 0$ (the velocity of the N_2 gas that has just sublimed is
641 zero).

642 **Acknowledgments**

643 The authors thank the NASA New Horizons team for their excellent work on a fantastic mission and their interest
 644 in this research. We also thank CNES for its support. Finally, the authors are very grateful to two anonymous reviewers
 645 for their exceptionally detailed comments which helped to improve the readability of the article.

646 **References**

- 647 Arakawa, A., Lamb, V. R., 1977. Computational design of the UCLA general circulation model. *Methods in Computational Physics* 17, 174–267.
- 648 Bertrand, T., Forget, F., 2016. 3D modeling of organic haze in Pluto s atmosphere . *Icarus*, this issue.
- 649 Bertrand, T., Forget, F., 2016. Observed glacier and volatile distribution on Pluto from atmospheretopography processes. *Nature* 19337.
- 650 Boursier, C., Menard, J., Doyennette, L., Menard-Bourcin, F., 2003. Rovibrational relaxation of methane in CH₄N₂ mixtures: Time-resolved IRIR
 651 doublingresonance measurements at 193 K and kinetic modeling . *J. Phys. Chem.* 107, 52805290.
- 652 Dias-Oliveira, A., Sicardy, B., Lellouch, E., Vieira-Martins, R., Assafin, M., Camargo, J. I. B., Braga-Ribas, F., Gomes-Júnior, A. R., Benedetti-
 653 Rossi, G., Colas, F., Decock, A., Doressoundiram, A., Dumas, C., Emilio, M., Fabrega Polleri, J., Gil-Hutton, R., Gillon, M., Girard, J. H., Hau,
 654 G. K. T., Ivanov, V. D., Jehin, E., Lecacheux, J., Leiva, R., Lopez-Sisterna, C., Mancini, L., Manfroid, J., Maury, A., Meza, E., Morales, N.,
 655 Nagy, L., Opatom, C., Ortiz, J. L., Pollock, J., Roques, F., Snodgrass, C., Soulier, J. F., Thirouin, A., Vanzi, L., Widemann, T., Reichart, D. E.,
 656 LaCluyze, A. P., Haislip, J. B., Ivarsen, K. M., Dominik, M., Jørgensen, U., Skottfelt, J., 2015. Pluto s Atmosphere from Stellar Occultations in
 657 2012 and 2013. *Astrophysical Journal* 811, 53.
- 658 Douté, S., Schmitt, B., Quirico, E., Owen, T. C., Cruikshank, D. P., de Bergh, C., Geballe, T. R., Roush, T. L., 1999. Evidence for Methane
 659 Segregation at the Surface of Pluto. *Icarus* 142, 421–444.
- 660 Elliot, J. L., Ates, A., Babcock, B. A., Bosh, A. S., Buie, M. W., Clancy, K. B., Dunham, E. W., Eikenberry, S. S., Hall, D. T., Kern, S. D., Leggett,
 661 S. K., Levine, S. E., Moon, D.-S., Olkin, C. B., Osip, D. J., Pasachoff, J. M., Penprase, B. E., Person, M. J., Qu, S., Rayner, J. T., Roberts, L. C.,
 662 Salyk, C. V., Souza, S. P., Stone, R. C., Taylor, B. W., Tholen, D. J., Thomas-Osip, J. E., Ticehurst, D. R., Wasserman, L. H., 2003a. The recent
 663 expansion of Pluto’s atmosphere. *Nature* 424, 165–168.
- 664 Elliot, J. L., Ates, A., Babcock, B. A., Bosh, A. S., Buie, M. W., Clancy, K. B., Dunham, E. W., Eikenberry, S. S., Hall, D. T., Kern, S. D., Leggett,
 665 S. K., Levine, S. E., Moon, D.-S., Olkin, C. B., Osip, D. J., Pasachoff, J. M., Penprase, B. E., Person, M. J., Qu, S., Rayner, J. T., Roberts, L. C.,
 666 Salyk, C. V., Souza, S. P., Stone, R. C., Taylor, B. W., Tholen, D. J., Thomas-Osip, J. E., Ticehurst, D. R., Wasserman, L. H., 2003b. The recent
 667 expansion of Pluto’s atmosphere. *Nature* 424, 165–168.
- 668 Elliot, J. L., Dunham, E. W., Bosh, A. S., Slivan, S. M., Young, L. A., Wasserman, L. H., Millis, R. L., 1989. Pluto’s atmosphere. *Icarus* 77,
 669 148–170.
- 670 Elliot, J. L., Person, M. J., Gulbis, A. A. S., Souza, S. P., Adams, E. R., Babcock, B. A., Gangestad, J. W., Jaskot, A. E., Kramer, E. A., Pasachoff,
 671 J. M., Pike, R. E., Zuluaga, C. A., Bosh, A. S., Dieters, S. W., Francis, P. J., Giles, A. B., Greenhill, J. G., Lade, B., Lucas, R., Ramm, D. J.,
 672 2007. Changes in Pluto’s Atmosphere: 1988-2006. *Astrophys. Jour.* 134, 1–13.
- 673 Forget, F., Haberle, R. M., Montmessin, F., Levrard, B., Head, J. W., 2006. Formation of Glaciers on Mars by Atmospheric Precipitation at High
 674 Obliquity. *Science* 311, 368–371.
- 675 Forget, F., Hourdin, F., Fournier, R., Hourdin, C., Talagrand, O., Collins, M., Lewis, S. R., Read, P. L., Huot, J.-P., 1999. Improved general
 676 circulation models of the Martian atmosphere from the surface to above 80 km. *J. Geophys. Res.* 104, 24,155–24,176.
- 677 Forget, F., Hourdin, F., Talagrand, O., 1998. CO₂ snow fall on Mars: Simulation with a general circulation model. *Icarus* 131, 302–316.

- 678 Fray, N., Schmitt, B., 2009. Sublimation of ices of astrophysical interest: A bibliographic review. *Planet. Space Sci.* 57, 2053–2080.
- 679 Gierasch, P. J., 1975. Meridional circulation and the maintenance of the Venus atmospheric rotation. *J. Atmos. Sci.* 32, 1038–1044.
- 680 Gladstone, G. R., Stern, S. A., Ennico, K., Olkin, C. B., Weaver, H. A., Young, L. A., Summers, M. E., Strobel, D. F., Hinson, D. A., Kammer,
681 J. A., Parker, A. H., Steffl, A. J., Linscott, I. R., Parker, J. W., Cheng, A. F., Slater, D. C., Versteeg, M. H., Greathouse, T. K., Retherford, K. D.,
682 Throop, H., Cunningham, N. J., Woods, W. W., Singer, K. N., Tsang, C. C. C., Schindhelm, E., Lisse, C. M., Wong, M. L., Yung, Y. L., Zhu,
683 X., Curdt, W., Lavvas, P., Young, E. F., Tyler, G. L., 2016. The Atmosphere of Pluto as observed by New Horizons. *Science* 351, 1280.
- 684 González-Galindo, F., Forget, F., López-Valverde, M. A., Angelats i Coll, M., Millour, E., 2009. A Ground-to-Exosphere Martian General Cir-
685 culation Model. I. Seasonal, Diurnal and Solar Cycle Variation of Thermospheric Temperatures. *Journal of Geophysical Research (Planets)*
686 114 (E13), 4001.
- 687 Grundy, W. M., Binzel, R. P., Buratti, B. J., Cook, J. C., Cruikshank, D. P., DalleOre, C. M., Earle, M., Ennico, K., Howett, C. J. A., Lunsford,
688 A. W., Olkin, C. B., Parker, A. H., Philippe, S., Protopapa, S., Quirico, E., Reuter, D. C., Schmitt, B., Singer, K. N., Verbiscer, A. J., Beyer,
689 R. A., Buie, M. W., Cheng, A. F., Jennings, D. E., Linscott, I. R., Parker, J. W., Schenk, P. M., Spencer, J. R., Stansberry, J. A., Stern, S. A.,
690 Throop, H. B., Tsang, C. C. C., Weaver, H. A., Weigle II, G. E., Young, L. A., 2016. Surface compositions across Pluto and Charon. *Science*
691 351, 1283.
- 692 Grundy, W. M., Olkin, C. B., Young, L. A., Buie, M. W., Young, E. F., Apr. 2013. Near-infrared spectral monitoring of Pluto's ices: Spatial
693 distribution and secular evolution. *Icarus* 223, 710–721.
- 694 Gurwell, M., Lellouch, E., Butler, B., Moullet, A., Moreno, R., Bockelée-Morvan, D., Biver, N., Fouchet, T., Lis, D., Stern, A., Young, L., Young,
695 E., Weaver, H., Boissier, J., Stansberry, J., 2015. Detection of Atmospheric CO on Pluto with ALMA. In: AAS/Division for Planetary Sciences
696 Meeting Abstracts. Vol. 47 of AAS/Division for Planetary Sciences Meeting Abstracts. p. 105.06.
- 697 Hansen, C. J., Paige, D. A., 1996. Seasonal Nitrogen Cycles on Pluto. *Icarus* 120, 247–265.
- 698 Hinson, D. P., Linscott, I., Tyler, G. L., Bird, M. K., Paetzold, M., Strobel, D. F., Summers, M. E., Woods, W. W., Stern, A., Weaver, Jr.,
699 H. A., Olkin, C., Young, L. A., Ennico Smith, K., Gladstone, R., Greathouse, T., Kammer, J., Parker, A. H., Parker, J. W., Retherford, K. D.,
700 Schindhelm, E., Singer, K. N., Steffl, A., Tsang, C., Versteeg, M., Dec. 2015a. Radio Occultation Measurements of Pluto's Atmosphere with
701 New Horizons. AGU Fall Meeting Abstracts.
- 702 Hinson, D. P., Linscott, I., Tyler, L., Bird, M., Paetzold, M., Strobel, D., Summers, M., Woods, W., Stern, A., Weaver, H., Olkin, C., Young, L.,
703 Ennico, K., Gladstone, R., Greathouse, T., Kammer, J., Parker, A., Parker, J., Retherford, K., Schindhelm, E., Singer, K., Steffl, A., Tsang,
704 C., Versteeg, M., Nov. 2015b. Radio Occultation Measurements of Pluto's Atmosphere with New Horizons. In: AAS/Division for Planetary
705 Sciences Meeting Abstracts. Vol. 47, p. 105.01.
- 706 Hourdin, F., Armengaud, A., 1999. Test of a hierarchy of finite-volume schemes for transport of trace species in an atmospheric general circulation
707 model. *Mon. Wea. Rev.* 127, 822–837.
- 708 Hourdin, F., Forget, F., Talagrand, O., 1995. The sensitivity of the Martian surface pressure to various parameters: A comparison between numerical
709 simulations and Viking observations. *J. Geophys. Res.* 100, 5501–5523.
- 710 Hubbard, W. B., Hunten, D. M., Dieters, S. W., Hill, K. M., Watson, R. D., 1988. Occultation evidence for an atmosphere on Pluto. *Nature* 336,
711 452–454.
- 712 Hubbard, W. B., Yelle, R. V., Lunine, J. I., 1990. Nonisothermal Pluto atmosphere models. *Icarus* 84, 1–11.
- 713 Lebonnois, S., Burgalat, J., Rannou, P., Charnay, B., 2012. Titan global climate model: A new 3-dimensional version of the IPSL Titan GCM.
714 *Icarus* 218, 707–722.
- 715 Lebonnois, S., Hourdin, F., Eymet, V., Cresspin, A., Fournier, R., Forget, F., 2010. Superrotation of Venus' atmosphere analyzed with a full general
716 circulation model. *Journal of Geophysical Research (Planets)* 115, 6006.

- 717 Lellouch, E., de Bergh, C., Sicardy, B., Forget, F., Vangvichith, M., Käufel, H.-U., 2015. Exploring the spatial, temporal, and vertical distribution of
718 methane in Pluto's atmosphere. *Icarus* 246, 268–278.
- 719 Lellouch, E., de Bergh, C., Sicardy, B., Käufel, H. U., Smette, A., 2011a. High resolution spectroscopy of Pluto's atmosphere: detection of the 2.3
720 μm CH_4 bands and evidence for carbon monoxide. *Astron. Astrophys.* 530, L4.
- 721 Lellouch, E., Gurwell, M., Butler, B., Fouchet, T., Lavvas, P., Strobel, D. F., Sicardy, B., Moullet, A., Moreno, R., Bockelée-Morvan, D., Biver, N.,
722 Young, L., Lis, D., Stansberry, J., Stern, A., Weaver, H., Young, E., Zhu, X., Boissier, J., 2016. Detection of CO and HCN in Pluto's atmosphere
723 with ALMA. *Icarus*, in press.
- 724 Lellouch, E., Sicardy, B., de Bergh, C., Käufel, H.-U., Kassi, S., Campargue, A., 2009. Pluto's lower atmosphere structure and methane abundance
725 from high-resolution spectroscopy and stellar occultations. *Astron. Astrophys.* 495, L17–L21.
- 726 Lellouch, E., Stansberry, J., Emery, J., Grundy, W., Cruikshank, D. P., 2011b. Thermal properties of Pluto's and Charon's surfaces from Spitzer
727 observations. *Icarus* 214, 701–716.
- 728 Mellor, G. L., Yamada, T., November 1982. Development of a turbulence closure model for geophysical fluid problems. *Rev. of Geophys.* 20 (4),
729 851–875.
- 730 Merlin, F., 2015. New constraints on the surface of Pluto. *Astron. Astrophys.* 582, A39.
- 731 Moore, J. M., McKinnon, W. B., Spencer, J. R., Howard, A. D. Schenk, P. M., Beyer, R. A., Nimmo, F., Singer, K. N., Umurhan, O. M., White,
732 O. L., Stern, S. A., Ennico, K. Olkin, C. B., Weaver, H. A., Young, L. A., Binzel, R. P., Buie, M. W., Buratti, B. J., Cheng, A. F., Cruikshank,
733 D. P., Grundy, W. M., Linscott, I. R., Reitsema, H. J., Reuter, D. C. Showalter, M. P., Bray, V. J., Chavez, C. L., Howett, C. J. A., Lauer, T. R.,
734 Lisse, C. M., Parker, A. H., Porter, S. B. Robbins, S. J., Runyon, K., Stryk, T., Throop, H. B. Tsang, C. C. C., Verbiscer, A. J., Zangari, A.
735 M. Chaikin, A. L., Wilhelms, D. E., 2016. The geology of Pluto and Charon through the eyes of New Horizons . *Science* 351, 1284.
- 736 Olkin, C. B., Young, L. A., Borncamp, D., Pickles, A., Sicardy, B., Assafin, M., Bianco, F. B., Buie, M. W., de Oliveira, A. D., Gillon, M., French,
737 R. G., Ramos Gomes, A., Jehin, E., Morales, N., Opitom, C., Ortiz, J. L., Maury, A., Norbury, M., Braga-Ribas, F., Smith, R., Wasserman,
738 L. H., Young, E. F., Zacharias, M., Zacharias, N., 2015. Evidence that Pluto's atmosphere does not collapse from occultations including the
739 2013 May 04 event. *Icarus* 246, 220–225.
- 740 Owen, T. C., Roush, T. L., Cruikshank, D. P., Elliot, J. L., Young, L. A., de Bergh, C., Schmitt, B., Geballe, T. R., Brown, R. H., Bartholomew,
741 M. J., 1993. Surface ices and the atmospheric composition of Pluto. *Science* 261, 745–748.
- 742 Person, M. J., Elliot, J. L., Gulbis, A. A. S., Zuluaga, C. A., Babcock, B. A., McKay, A. J., Pasachoff, J. M., Souza, S. P., Hubbard, W. B., Kulesa,
743 C. A., McCarthy, D. W., Benecchi, S. D., Levine, S. E., Bosh, A. S., Ryan, E. V., Ryan, W. H., Meyer, A., Wolf, J., Hill, J., 2008. Waves in
744 Pluto's Upper Atmosphere. *Astron. Jour.* 136, 1510–1518.
- 745 Rossow, W. B., 1978. Cloud microphysics: Analysis of the clouds of Earth, Venus, Mars, and Jupiter. *Icarus* 36, 1,50.
- 746 Rossow, W. B., 1979. Large-scale motion in the Venus stratosphere. *J. Atmos. Sci.* 36, 377–389.
- 747 Sicardy, B., Talbot, J., Meza, E., Camargo, J. I. B., Desmars, J., Gault, D., Herald, D., Kerr, S., Pavlov, H., Braga-Ribas, F., Assafin, M., Benedetti-
748 Rossi, G., Dias-Oliveira, A., Ramos-Gomes-Jr., A., Vieira-Martins, R., Berard, D., Kervella, P., Lecacheux, J., Lellouch, E., Beisker, W.,
749 Dunham, D., Jelinek, M., Duffard, R., Ortiz, J. L., Castro-Tirado, A. J., Cunniffe, R., Querel, R., Yock, P. A., Cole, A. A., Giles, A. B., Hill,
750 K. M., Beaulieu, J. P., Harnisch, M., Jansen, R., Pennell, A., Todd, S., Allen, W. H., Graham, P. B., Loader, B., McKay, G., Milner, J., Parker,
751 S., Barry, M. A., Bradshaw, J., Broughton, J., Davis, L., Devillepoix, H., Drummond, J., Field, L., Forbes, M., Giles, D., Glassey, R., Groom,
752 R., Hooper, D., Horvat, R., Hudson, G., Idaczyk, R., Jenke, D., Lade, B., Newman, J., Nosworthy, P., Purcell, P., Skilton, P. F., Streamer, M.,
753 Unwin, M., Watanabe, H., White, G. L., Watson, D., 2016. Pluto's atmosphere from the 29 June 2015 ground-based stellar occultation at the
754 time of the New Horizons flyby. *The Astrophysical Journal Letters* 819, L38.
- 755 Stern, S. A., Bagenal, F., Ennico, K., Gladstone, G. R., Grundy, W. M., McKinnon, W. B., Moore, J. M., Olkin, C. B., Spencer, J. R., Weaver, H. A.,

- 756 Young, L. A., Andert, T., Andrews, J., Banks, M., Bauer, B., Bauman, J., Barnouin, O. S., Bedini, P., Beisser, K., Beyer, R. A., Bhaskaran,
757 S., Binzel, R. P., Birath, E., Bird, M., Bogan, D. J., Bowman, A., Bray, V. J., Brozovic, M., Bryan, C., Buckley, M. R., Buie, M. W., Buratti,
758 B. J., Bushman, S. S., Calloway, A., Carcich, B., Cheng, A. F., Conard, S., Conrad, C. A., Cook, J. C., Cruikshank, D. P., Custodio, O. S.,
759 Dalle Ore, C. M., Deboy, C., Dischner, Z. J. B., Dumont, P., Earle, A. M., Elliott, H. A., Ercol, J., Ernst, C. M., Finley, T., Flanigan, S. H.,
760 Fountain, G., Freeze, M. J., Greathouse, T., Green, J. L., Guo, Y., Hahn, M., Hamilton, D. P., Hamilton, S. A., Hanley, J., Harch, A., Hart, H. M.,
761 Hersman, C. B., Hill, A., Hill, M. E., Hinson, D. P., Holdridge, M. E., Horanyi, M., Howard, A. D., Howett, C. J. A., Jackman, C., Jacobson,
762 R. A., Jennings, D. E., Kammer, J. A., Kang, H. K., Kaufmann, D. E., Kollmann, P., Krimigis, S. M., Kusnierkiewicz, D., Lauer, T. R., Lee,
763 J. E., Lindstrom, K. L., Linscott, I. R., Lisse, C. M., Lunsford, A. W., Mallder, V. A., Martin, N., McComas, D. J., McNutt, R. L., Mehoke,
764 D., Mehoke, T., Melin, E. D., Mutchler, M., Nelson, D., Nimmo, F., Nunez, J. I., Ocampo, A., Owen, W. M., Paetzold, M., Page, B., Parker,
765 A. H., Parker, J. W., Pelletier, F., Peterson, J., Pinkine, N., Piquette, M., Porter, S. B., Protopapa, S., Redfern, J., Reitsema, H. J., Reuter, D. C.,
766 Roberts, J. H., Robbins, S. J., Rogers, G., Rose, D., Runyon, K., Retherford, K. D., Ryschkewitsch, M. G., Schenk, P., Schindhelm, E., Sepan,
767 B., Showalter, M. R., Singer, K. N., Soluri, M., Stanbridge, D., Steffl, A. J., Strobel, D. F., Stryk, T., Summers, M. E., Szalay, J. R., Tapley, M.,
768 Taylor, A., Taylor, H., Throop, H. B., Tsang, C. C. C., Tyler, G. L., Umurhan, O. M., Verbiscer, A. J., Versteeg, M. H., Vincent, M., Webbert,
769 R., Weidner, S., Weigle, G. E., White, O. L., Whittenburg, K., Williams, B. G., Williams, K., Williams, S., Woods, W. W., Zangari, A. M.,
770 Zirnstein, E., 2015. The Pluto system: Initial results from its exploration by New Horizons. *Science* 350.
- 771 Strobel, D. F., Zhu, X., Summers, M. E., Stevens, M. H., 1996. On the Vertical Thermal Structure of Pluto's Atmosphere. *Icarus* 120, 266–289.
- 772 Toigo, A. D., French, R. G., Gierasch, P. J., Guzewich, S. D., Zhu, X., Richardson, M. I., 2015. General circulation models of the dynamics of
773 Pluto's volatile transport on the eve of the New Horizons encounter. *Icarus* 254, 306–323.
- 774 Toigo, A. D., Gierasch, P. J., Sicardy, B., Lellouch, E., 2010. Thermal tides on Pluto. *Icarus* 208, 402–411.
- 775 Van Leer, B., 1977. Towards the ultimate conservative difference scheme : IV. a new approach to numerical convection. *J. Computational Phys.* 23,
776 276–299.
- 777 Vangichith, M., Forget, F., Aug. 2011. Climate models of Triton and Pluto. New Horizons Workshop on Icy Surface Processes, Lowell Observatory,
778 Flagstaff Arizona 1447.
- 779 Yelle, R. V., Lunine, J. I., 1989. Evidence for a molecule heavier than methane in the atmosphere of Pluto. *Nature* 339, 288–290.
- 780 Young, E. F., French, R. G., Young, L. A., Ruhland, C. R., Buie, M. W., Olkin, C. B., Regester, J., Shoemaker, K., Blow, G., Broughton, J., Christie,
781 G., Gault, D., Lade, B., Natusch, T., 2008. Vertical Structure in Pluto's Atmosphere from the 2006 June 12 Stellar Occultation. *Astron. Jour.*
782 136, 1757–1769.
- 783 Young, L. A., 2013. Pluto's Seasons: New Predictions for New Horizons. *Astrophysical Journal* 766, L22.
- 784 Young, L. A., Elliot, J. L., Tokunaga, A., de Bergh, C., Owen, T., 1997. Detection of Gaseous Methane on Pluto. *Icarus* 127, 258.
- 785 Zalucha, A. M., 2016. An atmospheric general circulation model for Pluto with predictions for New Horizons temperature profiles. *Monthly Notices*
786 of the Royal Astronomical Society 459, 902–923.
- 787 Zalucha, A. M., Gulbis, A. A. S., Zhu, X., Strobel, D. F., Elliot, J. L., 2011. An analysis of Pluto occultation light curves using an atmospheric
788 radiative-convective model. *Icarus* 211, 804–818.
- 789 Zalucha, A. M., Michaels, T. I., 2013. A 3D general circulation model for Pluto and Triton with fixed volatile abundance and simplified surface
790 forcing. *Icarus* 223, 819–831.